IMMUNOLOGY

Inflammation of the retinal pigment epithelium drives early-onset photoreceptor degeneration in *Mertk*-associated retinitis pigmentosa

Maria E. Mercau[1]†, Yemsratch T. Akalu[1]†, Francesca Mazzoni[2], Gavin Gyimesi[2], Emily J. Alberto[1], Yong Kong[3], Brian P. Hafler[4,5], Silvia C. Finnemann[2]*, Carla V. Rothlin[1,6]*, Sourav Ghosh[6,7]*

Severe, early-onset photoreceptor (PR) degeneration associated with *MERTK* mutations is thought to result from failed phagocytosis by retinal pigment epithelium (RPE). Notwithstanding, the severity and onset of PR degeneration in mouse models of *Mertk* ablation are determined by the hypomorphic expression or the loss of the *Mertk* paralog *Tyro3*. Here, we find that loss of *Mertk* and reduced expression/loss of *Tyro3* led to RPE inflammation even before eye-opening. Incipient RPE inflammation cascaded to involve microglia activation and PR degeneration with monocyte infiltration. Inhibition of RPE inflammation with the JAK1/2 inhibitor ruxolitinib mitigated PR degeneration in *Mertk*$^{-/-}$ mice. Neither inflammation nor severe, early-onset PR degeneration was observed in mice with defective phagocytosis alone. Thus, inflammation drives severe, early-onset PR degeneration–associated with *Mertk* loss of function.

INTRODUCTION

Retinitis pigmentosa (RP) is a group of heterogeneous degenerative diseases that lead to rod and cone photoreceptor (PR) dystrophy, night blindness, progressive visual field constriction, and, ultimately, central vision loss (*1*). RP is known to be primarily a hereditary disorder with over 45 different genes implicated (*2*). One such gene is *MERTK* (*3*), a member of the TAM (*Tyro3*, *Axl*, and *Mertk*) subfamily of receptor tyrosine kinases (RTKs). RP associated with *MERTK* mutations is usually severe and has been observed in patients as early as 3 years of age (*3–6*). Macular involvement is rapid (*3*, *4*). Severe, early-onset retinal degeneration is also observed in a laboratory model of spontaneous inherited retinal degeneration, the Royal College of Surgeons' (RCS) rat (*7*). RCS rats develop normal vision with no detectable differences in electroretinogram (ERG) at postnatal day 15 (P15) (*7*). ERG changes are detected in RCS rats by P18, and animals are completely blind by P60 (*7*). In vitro phagocytosis assays using retinal pigment epithelial (RPE) cells from RCS rats revealed defective engulfment of PR outer segment (POS) fragments in comparison to RPE cells derived from wild-type (WT) rats (*8*). It was found that the RCS rat carries a ~1.5-kb deletion that includes the *Mertk* locus (*9*, *10*) and that MERTK was required for RPE phagocytosis (*11*). The genetic targeting and ablation of *Mertk* in 129P2/OLAHsd (129) embryonic stem cell–derived mice (henceforth referred to as

Mertk$^{-/-V1}$ mice) result in a similar, severe, early-onset retinal degeneration (*12*). ERG recordings revealed that *Mertk*$^{-/-V1}$ mice displayed early signs of impairment in retinal function at P20 when compared to WT mice (*12*). On the basis of these observations, it is postulated that the failure of POS fragments engulfment and the accumulation of POS fragment debris due to the absence of *Mertk* result in PR degeneration in *Mertk*$^{-/-V1}$ mice. Nonetheless, not all *MERTK* mutations have a severe, early-onset phenotype. For example, Tschernutter *et al.* (*5*) identified a family with a milder form of *MERTK* mutation–associated RP. In addition, two missense *MERTK* mutations were found in a patient with RP, but the mother, who had identical mutations, was unaffected (*13*). Such findings raise the possibility that genetic modifiers may determine the severity of RP and time to vision loss.

RPE cells express, in addition to MERTK, other phagocytic receptors such as αvβ5 integrin (*14*) and CD81, which acts as an integrin coreceptor (*15*). The MERTK paralog TYRO3 is also expressed in the RPE (*16*, *17*) and indicated to have a functional role in POS fragments uptake (*17*). Intriguingly, not all mouse models with genetic ablation of phagocytic receptors display the severe, early-onset retinal degeneration phenotype observed in *Mertk*$^{-/-V1}$ mice. We have previously demonstrated that the *Itgb5*$^{-/-}$ mouse line exhibits substantial RPE phagocytosis defects in vivo and in vitro (*14*, *18*). Nonetheless, ERGs from *Itgb5*$^{-/-}$ and WT mice indicated that both mouse lines had comparable vision at 4 months of age (*14*). *Itgb5*$^{-/-}$ and WT retina gross morphology was intact even at 12 months of age; however, *Itgb5*$^{-/-}$ RPE accumulated excessive levels of lipofuscin and ERGs showed loss of PR function with age (*14*). CD81 blockade or silencing inhibited αvβ5 integrin and thus POS fragments uptake by cultured RPE (*15*). However, to date, there are no reports on PR degeneration in *Cd81*$^{-/-}$ mice. Instead, there was a modest increase in RPE cell and nuclear density and an increase in the number of multinucleated RPE in *Cd81*$^{-/-}$ eyes (*19*, *20*). Genetic ablation of the αvβ5 integrin ligand, MFG-E8, yielded the same phagocytic defects as in αvβ5 receptor–deficient mice but did not show lipofuscin or

[1]Department of Immunobiology, School of Medicine, Yale University, New Haven, CT 06520, USA. [2]Center for Cancer, Genetic Diseases and Gene Regulation, Department of Biological Sciences, Fordham University, Bronx, NY 10458, USA. [3]Department of Molecular Biophysics and Biochemistry, W. M. Keck Foundation Biotechnology Resource Laboratory, School of Medicine, Yale University, New Haven, CT 06520, USA. [4]Department of Ophthalmology, School of Medicine, Yale University, New Haven, CT 06520, USA. [5]Department of Pathology, School of Medicine, Yale University, New Haven, CT 06520, USA. [6]Department of Pharmacology, School of Medicine, Yale University, New Haven, CT 06520, USA. [7]Department of Neurology, School of Medicine, Yale University, New Haven, CT 06520, USA.
†These authors contributed equally to this work.
*Corresponding author. Email: finnemann@fordham.edu (S.C.F); carla.rothlin@yale.edu (C.V.R.); sourav.ghosh@yale.edu (S.G.)

vision decline by 12 months of age (*18*). Recently, POS phagosome processing by the RPE has been shown to depend on LC3 lipidation and Beclin1 but not on ULK1 (*21*). ERG recordings indicated a similar visual function in 3-month-old *Vmd2-cre*[+] *Atg5* [f/f] mice and control mice, although retinal function decreased in *Vmd2-cre*[+] *Atg5* [f/f] mice by 4 months of age (*21*). There was no sign of PR degeneration in *Vmd2-cre*[+] *Atg5* [f/f] mice by 6 months of age (*21*). Collectively, these data suggest that PR degeneration resulting from RPE phagocytosis defects is progressive and age related. By contrast, PR degeneration in the absence of MERTK is severe and early onset. Therefore, we hypothesized that MERTK may have additional role(s), distinct from its role in phagocytosis. In addition, we proposed that the impact of this function of MERTK on retinal physiology is influenced by modifiers and is crucial for the maintenance of retinal homeostasis.

We and others have identified either the concomitant hypomorphic expression of *Tyro3* (in *Mertk*[−/−V1] mice) or the loss of function of *Tyro3* (in *Mertk*[−/−V2] *Tyro3*[−/−V2] mice) as a modifier of severe, early-onset PR degeneration in mice with the loss of *Mertk* function (*17, 22*). Here, we show that RPE inflammation is a distinct feature associated with severe, early-onset PR degeneration in *Mertk*[−/−V1] and *Mertk*[−/−V2] *Tyro3*[−/−V2] mice. RPE inflammation is detected early, before histological evidence of retinal degeneration, and even before eye-opening. This initial RPE inflammation, subsequently, manifests as microglial activation and, ultimately, as monocytic infiltration into the retina. Neither severe, early-onset retinal degeneration nor exacerbated RPE inflammation is a feature of *Mertk*[−/−V2] mice or of mouse models with genetic ablation of phagocytic receptors such as *Tyro3*[−/−V1] or *Itgb5*^{−/−} mice. The fact that, in *Mertk*[−/−V1] and *Mertk*[−/−V2] *Tyro3*[−/−V2] mice, RPE inflammation is detected as early as P10, when POS fragments phagocytosis is minimal in rodents, together with the lack of exaggerated inflammation in *Mertk*[−/−V2], *Tyro3*[−/−V1], or *Itgb5*^{−/−} mice, indicates that this inflammation is not a consequence of failed POS fragments phagocytosis. *Mertk* and *Tyro3* are well-characterized negative regulators of inflammatory cytokine signaling such as type I and II interferons (IFNs), interleukin-6 (IL-6), and tumor necrosis factor–α (TNF-α). Treatment with ruxolitinib, a Food and Drug Administration (FDA)–approved Janus kinase 1/2 (JAK1/2) inhibitor, of *Mertk*[−/−V1] mice resulted in successful partial preservation of the retinal histology, providing a proof of concept that inflammation is an important aspect of the etiology of severe, early-onset PR degeneration–associated with loss of function of *Mertk*. In conclusion, our results indicate that *Mertk* and *Tyro3* function redundantly in an anti-inflammatory mechanism in the RPE that is critical for retinal homeostasis. Targeting this inflammatory response in RP with severe, early-onset characteristics might provide a therapeutic avenue to mitigate disease progression.

RESULTS

Mertk[−/−V2] *Tyro3*[−/−V2] and *Mertk*[−/−V1] mice display severe, early-onset PR degeneration in contrast to progressive peripheral PR degeneration in *Mertk*[−/−V2] mice

We previously reported that *Mertk*[−/−V2] *Tyro3*[−/−V2] mice displayed retinal degeneration (*22*). To define the onset of PR degeneration in *Mertk*[−/−V2] *Tyro3*[−/−V2] mice, we histologically determined the outer nuclear layer (ONL) thickness at different postnatal time points, by hematoxylin and eosin (H&E) staining (Fig. 1).

Measurements were taken in areas representing the central, intermediate, and peripheral retina (Fig. 1A). We observed significant decrease in ONL thickness in *Mertk*[−/−V2] *Tyro3*[−/−V2] mice as compared to C57BL/6 (B6) WT mice at P35 (Fig. 1B). The decrease in ONL thickness in *Mertk*[−/−V2] *Tyro3*[−/−V2] mice was similar to that observed in *Mertk*[−/−V1] mice at P35. This decrease in ONL thickness in *Mertk*[−/−V2] *Tyro3*[−/−V2] mice, as compared to B6 WT mice, was also observed at P30 and was replicated in *Mertk*[−/−V1] mice at this age (Fig. 1B). However, ONL thickness at P25 was indistinguishable between B6 WT, *Mertk*[−/−V2] *Tyro3*[−/−V2], and *Mertk*[−/−V1] mice (Fig. 1B). These results indicate that the severity and onset of retinal degeneration in *Mertk*[−/−V2] *Tyro3*[−/−V2] and *Mertk*[−/−V1] mice were identical across the retina. Therefore, the loss of *Mertk* in the presence of the modifier hypomorphic expression or loss of function of *Tyro3* results in identical severe, early-onset PR degeneration.

We have recently generated an independent mouse line bearing *Mertk* ablation (termed *Mertk*[−/−V2] mice) (fig. S1) (*22*). Histological analyses of the retina from *Mertk*[−/−V2] mice revealed that there were no statistically significant differences of the central and intermediate portions of the retina of *Mertk*[−/−V2] mice by comparison to B6 WT, at P25, 6 months, or even at 12 months of age (Fig. 1C). Nonetheless, we did detect statistically significant differences between *Mertk*[−/−V2] and B6 WT mice in the peripheral retina (Fig. 1C). There was significant thinning of the peripheral retina, by comparison with B6 WT, at 6 and 12 months of age (Fig. 1C). Still, *Mertk*[−/−V2] mice did not display deficits in ERG responses even at 12 months of age (fig. S2, A to D). Retinal histology and ERG responses were also preserved in *Tyro3*[−/−V1] mice even at 1 year of age (Fig. 1D and fig. S2, A to D).

Together, our findings are consistent with those of Vollrath *et al.* (*17*) that demonstrated that, in *Mertk*^{−/−} *Tyro3*[B6/129] RPE, wherein TYRO3 expression was at 67% of *Tyro3*[B6/B6], the level of TYRO3 expression was enough to prevent severe, early-onset retinal degeneration. Severe, early-onset retinal degeneration was detected in *Mertk*^{−/−} *Tyro3*[B6/−] (TYRO3 amounts at 50% of *Tyro3*[B6/B6]) and progressively worsen in *Mertk*^{−/−} *Tyro3*[129/129] (TYRO3 amounts at ~33% of *Tyro3*[B6/B6]) and in *Mertk*^{−/−} *Tyro3*^{−/−} (*17*). *Mertk*^{−/−} *Tyro3*[B6/129] RPE did exhibit degeneration in the periphery (*17*), similar to our *Mertk*[−/−V2] mice. The age-related, progressive PR degeneration in *Mertk*[−/−V2] mice is also consistent with the observations of Maddox *et al.* (*23*), wherein an *N*-ethyl-*N*-nitrosourea mutagenesis that generated a homozygous *Mertk* [nmf12] mutation substituting a highly conserved histidine residue to arginine at amino acid position 716 within the tyrosine kinase domain and a 2.5-fold reduction in the amount of MERTK by immunoblotting failed to phenocopy the severe, early-onset PR degeneration of *Mertk*[−/−V1] mice. Instead, *Mertk* [nmf12]-mutated mice exhibited thinning of the peripheral ONL at P30, while the central retina was spared (*23*). ERG waveforms were detectable in *Mertk* [nmf12] homozygotes mice up to the age of 2 years (*23*). Thus, the loss of *Mertk* and the concomitant hypomorphic expression/simultaneous loss of *Tyro3* as in *Mertk*[−/−V1] and *Mertk*[−/−V2] *Tyro3*[−/−V2] mice, respectively, result in severe, early-onset PR degeneration. The loss of *Mertk* alone, as in *Mertk*[−/−V2] mice or the previously reported *Mertk*^{−/−} *Tyro3*[B6/129] (*17*) and *Mertk* [nmf12] mice (*23*), is associated with peripheral degeneration.
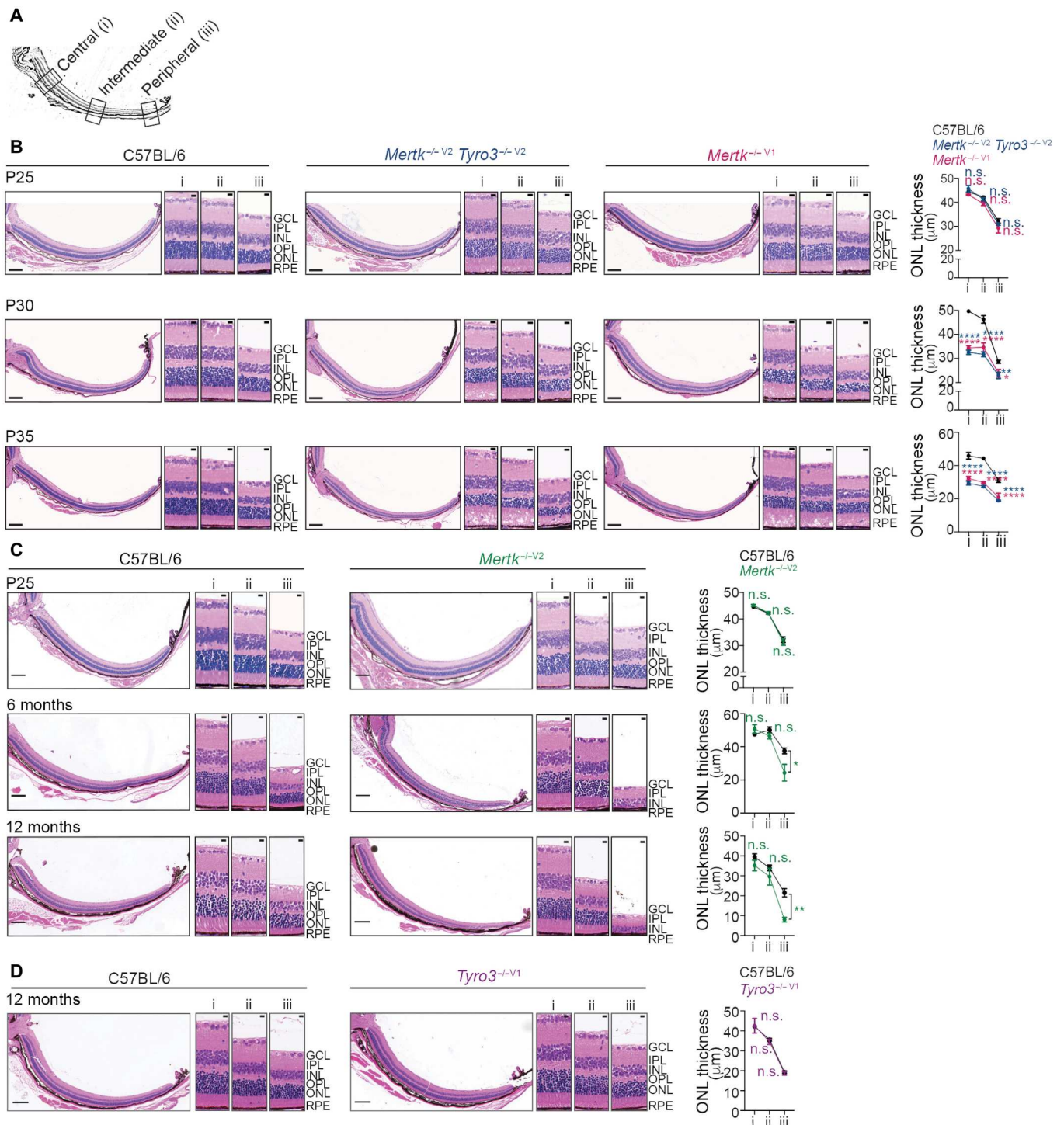
Fig. 1. Loss of *Mertk* and concomitant loss or hypomorphic expression of *Tyro3* leads to severe, early-onset PR degeneration. (**A**) Schematic of transversal section of the retina indicating the regions representing the central (i), intermediate (ii), and peripheral (iii) areas quantified to determine outer nuclear layer (ONL) thickness. (**B**) Transversal sections of P25, P30, and P35 C57BL/6 WT, *Mertk*$^{−/−V2}$ *Tyro3*$^{−/−V2}$, and *Mertk*$^{−/−V1}$ retina were stained with hematoxylin and eosin (H&E). Representative retinal sections and quantification of ONL thickness in central (i), intermediate (ii), and peripheral (iii) retinal areas are shown. Scale bars, 200 μm (whole section) and 10 μm (insets). *n* = 3 mice per genotype. (**C**) Transversal sections of P25, 6-month-old, and 12-month-old C57BL/6 WT and *Mertk*$^{−/−V2}$ retina were stained with H&E. Representative retinal sections and quantification of ONL thickness in central (i), intermediate (ii), and peripheral (iii) retinal areas are shown. *n* = 3 mice per genotype. (**D**) Transversal sections of 12-month-old C57BL/6 WT and *Tyro3*$^{−/−V1}$ retina were stained with H&E. Representative retinal sections and quantification of ONL thickness in central (i), intermediate (ii), and peripheral (iii) retinal areas are shown. Scale bars, 200 μm (whole section) and 10 μm (insets). *n* = 3 mice per genotype. All graphs represent means ± SEM of 15 measurements per area per mouse. n.s. (not significant), *$P < 0.05$, **$P < 0.01$, and ****$P < 0.0001$ versus C57BL/6 WT by two-way analysis of variance (ANOVA).

Inflammation is detected in the retina of $Mertk^{-/-V1}$ and $Mertk^{-/-V2}$ $Tyro3^{-/-V2}$ mice

Audo *et al.* (*3*) reported hyperreflective dots above the RPE/Bruch's membrane complex in all of their *MERTK* mutation–associated patients with RP. These hyperreflective dots were conjectured to be macrophages or activated microglia (*3*). Similarly, the increased number of fluorescent spots indicative of activated microglia was reported in $Mertk^{-/-V1}$ mice, and ionized calcium-binding adapter molecule 1 (IBA1)$^+$ cells were detected within the RPE and PR layers (*24*). Moreover, in the RCS rat, IBA1$^+$ cells were detected in the ONL at P30 (*25*). By P60, an increased number of IBA1$^+$ cells were detected across the entire retina, which decreased by P90 concurrently with the apoptosis of retinal cells (*25*). We have also previously reported that IBA1$^+$ microglial numbers are ~1.8-fold higher in the RCS rat than in WT rats between P14 and P30 and that RCS rat microglia migrate to the PR layer starting at P20 (*26*). Consistent with these observations, we noted the activation of resident immune cells and/or the infiltration of monocytes by flow cytometry analysis on the neural retina of $Mertk^{-/-V1}$, $Mertk^{-/-V2}$ $Tyro3^{-/-V2}$, and B6 WT mice (fig. S3). CD45$^+$ cells were defined as CD11b$^+$CD64$^+$Ly6C$^-$Ly6G$^-$ microglia or CD11b$^+$CD64$^-$Ly6C$^+$Ly6G$^-$ monocytes. At P42, there was a significantly larger number of CD45$^+$ cells in $Mertk^{-/-V1}$ and $Mertk^{-/-V2}$ $Tyro3^{-/-V2}$ retinas, relative to B6 WT retinas (fig. S3, A and C). We observed a statistically significant ~2.5-fold increase of CD45$^+$ cells in $Mertk^{-/-V1}$ retinas and ~3-fold increase of CD45$^+$ cells in $Mertk^{-/-V2}$ $Tyro3^{-/-V2}$ retinas, relative to B6 WT retinas. The number of CD45$^+$CD11b$^+$CD64$^+$Ly6C$^-$Ly6G$^-$ microglia expanded substantially by ~2.5-fold in $Mertk^{-/-V1}$ and 3-fold in $Mertk^{-/-V2}$ $Tyro3^{-/-V2}$ retinas, relative to B6 WT retinas (fig. S3, A and C). Similarly, CD45$^+$CD11b$^+$CD64$^-$Ly6C$^+$Ly6G$^-$ monocytes expanded by ~4-fold in $Mertk^{-/-V1}$ and 2-fold in $Mertk^{-/-V2}$ $Tyro3^{-/-V2}$ retinas, relative to B6 WT retinas (fig. S3, A and C). The microglia in $Mertk^{-/-V1}$ and $Mertk^{-/-V2}$ $Tyro3^{-/-V2}$ mice were activated, i.e., these cells expressed significantly higher amounts of activation markers such as CD68, CD11c, and GAL3, when compared to cells from B6 WT mice (fig. S3, B and D). In addition, CD68 and GAL3 expression levels were increased in CD11b$^+$CD64$^-$Ly6C$^+$Ly6G$^-$ monocytes from $Mertk^{-/-V1}$ and $Mertk^{-/-V2}$ $Tyro3^{-/-V2}$ mice, as compared to age-matched B6 WT mice (fig. S3E).

To test whether microglial activation and/or monocyte infiltration was observed in $Mertk^{-/-V1}$ and $Mertk^{-/-V2}$ $Tyro3^{-/-V2}$ retinas even at a time point in which retinal degeneration was histologically not yet observable, we performed similar flow cytometry analysis in the retina of P25 mice. Again, we detected a significant increase in the number of CD45$^+$ cells in the retinas of $Mertk^{-/-V1}$ (~4-fold) and $Mertk^{-/-V2}$ $Tyro3^{-/-V2}$ (~5-fold) versus B6 WT mice (Fig. 2, A and C). The number of microglia was correspondingly increased by ~3-fold in $Mertk^{-/-V1}$ and ~8-fold in $Mertk^{-/-V2}$ $Tyro3^{-/-V2}$ versus B6 WT retinas (Fig. 2, A and C). Moreover, the expression level of activation markers (CD68, CD11c, and CD86) was also significantly elevated in these cells isolated from $Mertk^{-/-V1}$ and $Mertk^{-/-V2}$ $Tyro3^{-/-V2}$ retinas relative to B6 WT controls (Fig. 2, B and D). Unlike at P42, CD45$^+$CD11b$^+$CD64$^-$ monocytes were not detectable at P25 (Fig. 2, A and C). In agreement with our flow cytometry findings at P25, immunofluorescence analysis of the total number of IBA1$^+$ cells showed a significant increase in the number of IBA1$^+$ cells in retinal sections collected

from P25 $Mertk^{-/-V1}$ and $Mertk^{-/-V2}$ $Tyro3^{-/-V2}$ mice relative to B6 WT controls (Fig. 2E). Furthermore, we observed increased translocation of microglia to the ONL layer in $Mertk^{-/-V1}$ and $Mertk^{-/-V2}$ $Tyro3^{-/-V2}$ mice. By contrast, 100% of IBA1$^+$ cells localized to the outer plexiform layer (OPL) in samples obtained from age matched B6 WT controls (Fig. 2E). In addition to flow cytometry and immunohistological analysis, we used Luminex multiplexed cytokine array analyses on P25 lysates of retina and RPE obtained from $Mertk^{-/-V1}$, $Mertk^{-/-V2}$, $Tyro3^{-/-V2}$, and B6 WT mice. This assay demonstrated elevated levels of the chemokine/cytokines CXCL10, CCL12, and CCL19; macrophage colony-stimulating factor (MCSF); and leukemia inhibitory factor (LIF) in $Mertk^{-/-V1}$ and $Mertk^{-/-V2}$ $Tyro3^{-/-V2}$ lysates by comparison to their B6 WT counterparts (Fig. 2F). Collectively, these results indicate that the absence of *Mertk* together with the hypomorphic expression/loss of *Tyro3* is associated with increased production of inflammatory cytokines and chemokines, microglial activation, and translocation from the OPL to the ONL by P25, an age at which no histological signs of retinal degeneration were detected. Thus, inflammation is a feature of two independent mouse models of severe, early-onset PR degeneration. Furthermore, like in the RCS rat, inflammation is not simply a consequence of retinal degeneration but is detected before histological changes are observed in $Mertk^{-/-V1}$ and $Mertk^{-/-V2}$ $Tyro3^{-/-V2}$ retina.

RPE inflammation is a distinct hallmark of $Mertk^{-/-V1}$ and $Mertk^{-/-V2}$ $Tyro3^{-/-V2}$ mice but not a general feature of mice with genetic ablation of phagocytosis receptors

Albeit microglia are activated in the two models of severe, early-onset PR degeneration, both these models require the loss of *Mertk* together with the hypomorphic expression/loss of *Tyro3*. Microglia, however, express only *Mertk* and do not express *Tyro3*. Unlike microglia, RPE coexpresses *Mertk* and *Tyro3* (*16, 17, 22*). Therefore, we tested whether there was an RPE-intrinsic inflammatory response in the $Mertk^{-/-V1}$ and $Mertk^{-/-V2}$ $Tyro3^{-/-V2}$ mice. We performed unbiased transcriptomics to compare the gene expression landscape of isolated RPE cells from B6 WT, $Mertk^{-/-V1}$ and $Mertk^{-/-V2}$ $Tyro3^{-/-V2}$ mice at P25 (Fig. 3). Pairwise comparison of RNA sequencing (RNA-seq) data revealed 67 differentially expressed genes (DEGs) between $Mertk^{-/-V1}$ and B6 WT RPE (Fig. 3A). The differentially up-regulated genes in $Mertk^{-/-V1}$ compared to B6 WT RPE corresponded to pathways related to innate immune response, response to IFN-α and IFN-γ, and response to TNF-α, among other immune-related categories (Fig. 3B). To gain a broader understanding of the transcriptional changes in $Mertk^{-/-V1}$ versus B6 WT RPE, we performed gene set enrichment analysis (GSEA). This analysis also revealed pathways involved in the response to the inflammatory cytokines IFN-α, IFN-γ, IL-6, and TNF-α as top enriched categories in $Mertk^{-/-V1}$ RPE in comparison to B6 WT RPE (Fig. 3C). GSEA histograms for these categories showed increased enrichment score (ES), as well as a higher contribution of genes with higher signal-to-noise ratio in samples derived from $Mertk^{-/-V1}$ RPE cells relative to B6 WT (Fig. 3C). Similar to $Mertk^{-/-V1}$ RPE cells, we found 102 DEGs in $Mertk^{-/-V2}$ $Tyro3^{-/-V2}$ RPE when compared to B6 WT control RPE (Fig. 3D). The top enriched categories corresponding to the significantly up-regulated genes in $Mertk^{-/-V2}$ $Tyro3^{-/-V2}$ RPE versus B6 WT RPE were immune response–related categories, similar to what was observed for the genes significantly up-
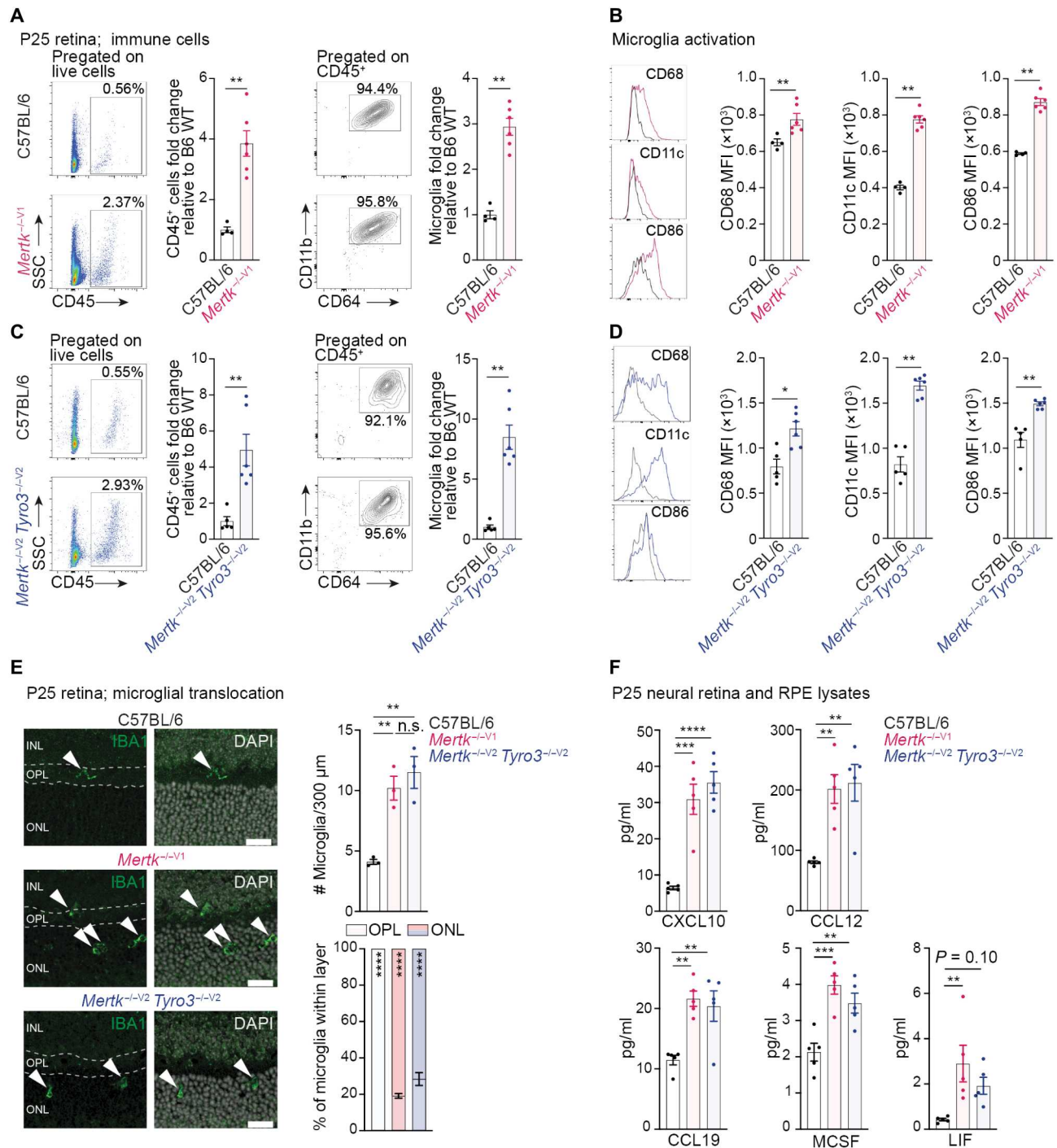
Fig. 2. Loss of *Mertk* and hypomorphic expression or concomitant loss of *Tyro3* leads to retinal inflammation. (**A**) Number of CD45+ cells and microglia (CD45+ CD11b+ CD64+ cells) in P25 C57BL/6 WT and *Mertk*−/−V1 retina, determined by flow cytometry. Represented as fold change versus C57BL/6 WT. *n* = 4 to 6 per group, Mann-Whitney's test. (**B**) Microglial expression of CD68, CD11c, and CD86 and corresponding quantification of mean fluorescence intensity (MFI). *n* = 4 to 6 per group, Mann-Whitney's test. (**C**) Number of CD45+ cells and microglia in P25 C57BL/6 WT and *Mertk*−/−V2 *Tyro3*−/−V2 retina, determined by flow cytometry. Represented as fold change versus C57BL/6 WT. *n* = 5 to 6 per group, Mann-Whitney's test. (**D**) Microglial expression of CD68, CD11c, and CD86 and corresponding MFI quantification. *n* = 5 to 6 per group, Mann-Whitney's test. (**E**) Representative IBA1 staining, indicating microglia localization (arrowheads) in P25 C57BL/6 WT, *Mertk*−/−V1, and *Mertk*−/−V2 *Tyro3*−/−V2 retina. Scale bars, 20 μm. Quantification of total number of IBA1+ cells. *n* = 3 per group, one-way ANOVA, Tukey's test. Percentage of IBA1+ cells in ONL versus OPL. *n* = 3 per group, two-way ANOVA. INL, inner nuclear layer; OPL, outer plexiform layer. (**F**) Quantification of chemokines and cytokines in neural retina and RPE lysates of P25 C57BL/6 WT, *Mertk*−/−V1, and *Mertk*−/−V2 *Tyro3*−/−V2 mice by Luminex. Represented as fold change versus C57BL/6 WT. *n* = 5 per genotype, one-way ANOVA, Dunnet's test. All bar graphs represent means ± SEM. *P < 0.05, **P < 0.01, ***P < 0.001, and ****P < 0.0001.
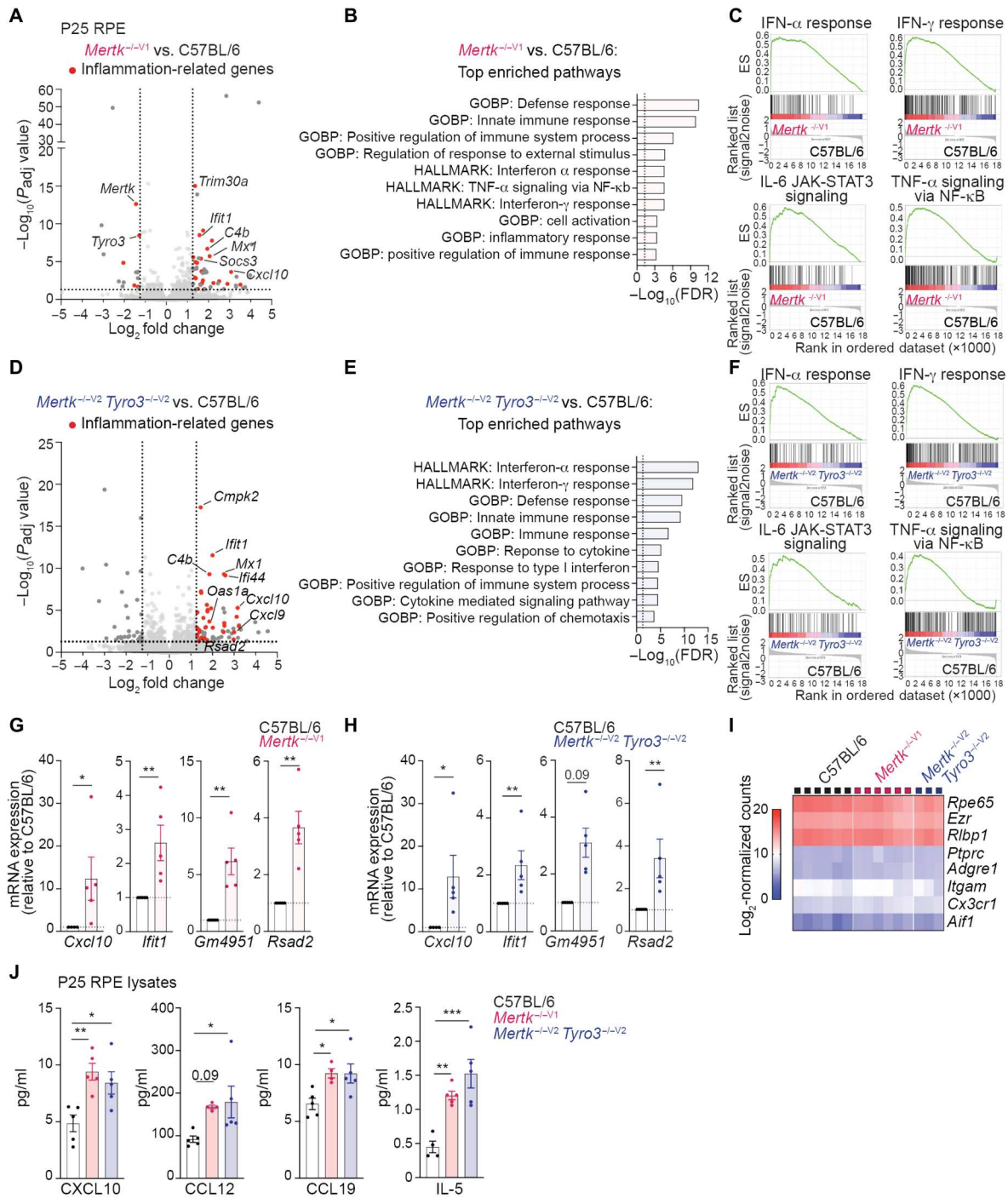
Fig. 3. Loss of *Mertk* and hypomorphic expression or concomitant loss of *Tyro3* triggers exacerbated inflammation in the RPE. (**A**) Volcano plot of gene expression in P25 *Mertk*[−/−V1] versus C57BL/6 WT RPE by RNA-seq (*n* = 6 per genotype, two animals pooled per sample). Significance: fold change > 2 or <−2 and *P*adj < 0.05. Inflammation-associated genes are indicated in red. (**B**) Top Gene Ontology Biological Orocess (GOBP) and HALLMARK pathways composed of genes significantly up-regulated (FDR < 0.05) in *Mertk*[−/−V1] versus C57BL/6 WT RPE at P25. (**C**) Gene set enrichment analysis (GSEA) comparing *Mertk*[−/−V1] versus C57BL/6 WT RPE. Significantly up-regulated categories in *Mertk*[−/−V1] mice are shown. ES, enrichment score. NF-κB, nuclear factor κB. (**D**) Volcano plot of gene expression in P25 *Mertk*[−/−V2] *Tyro3*[−/−V2] versus C57BL/6 WT RPE by RNA-seq (*n* = 3 to 6 per genotype, two animals pooled per sample). Significance: fold change > 2 or <−2 and *P*adj < 0.05. Inflammation-associated genes are indicated in red. (**E**) Top GOBP and HALLMARK pathways composed of genes significantly up-regulated (FDR < 0.05) in *Mertk*[−/−V2] *Tyro3*[−/−V2] versus C57BL/6 WT RPE at P25. (**F**) GSEA comparing *Mertk*[−/−V2] *Tyro3*[−/−V2] versus C57BL/6 WT RPE. Significantly up-regulated categories in *Mertk*[−/−V2] *Tyro3*[−/−V2] mice are shown. (**G** and **H**) qPCR validation of inflammation-associated genes up-regulated in *Mertk*[−/−V1] (G) or *Mertk*[−/−V2] *Tyro3*[−/−V2] (H) versus C57BL/6 WT RPE. *n* = 5 per genotype, Mann-Whitney's test. (**I**) Heatmap indicating log₂-normalized counts of RPE- and immune cell–associated genes. P25 C57BL/6 WT, *Mertk*[−/−V1], and *Mertk*[−/−V2] *Tyro3*[−/−V2] RPE. (**J**) Levels of chemokines and cytokines in lysates of P25 C57BL/6 WT, *Mertk*[−/−V1], and *Mertk*[−/−V2] *Tyro3*[−/−V2] RPE by Luminex. Represented as fold change versus C57BL/6 WT. *n* = 4 to 5 per genotype, ANOVA, Dunnet's test. Bar graphs in (G), (H), and (J) represent means ± SEM. *P < 0.05, **P < 0.01, and ***P < 0.001.

regulated in $Mertk^{-/-V1}$ RPE (Fig. 3E). Consistently, GSEA of RPE RNA-seq data identified genes associated with the response to IFN-α, IFN-γ, IL-6, and TNF-α to be significantly enriched in $Mertk^{-/-V2}$ $Tyro3^{-/-V2}$ RPE compared to B6 WT RPE (Fig. 3F). Similar to $Mertk^{-/-V1}$ RPE, these GSEA categories showed higher ES, determined by genes with higher signal-to-noise ratio in samples derived from $Mertk^{-/-V2}$ $Tyro3^{-/-V2}$ RPE relative to B6 WT (Fig. 3F). We validated the differential expression of inflammatory response signaling genes, such as $Cxcl10$, $Ifit1$, $Gm4951$, and $Rsad2$, in $Mertk^{-/-V1}$ and $Mertk^{-/-V2}$ $Tyro3^{-/-V2}$ RPE by quantitative polymerase chain reaction (qPCR; Fig. 3, G and H). To confirm that these changes were stemming primarily from RPE cells and not from contaminating immune cells, we determined the expression of candidate RPE-specific versus immune cell–specific genes in our dataset. We found that, compared to counts for pan-immune cell marker CD45 ($Ptprc$), macrophage markers F4/80 ($Adgre1$) and CD11b ($Itgam$), and microglia markers CX3CR1 ($Cx3cr1$) and IBA-1 ($Aif1$), RPE genes $Rpe65$, Ezr, and $Rlbp1$ were enriched by >200-fold (Fig. 3I). This enrichment of RPE genes allowed us to attribute the inflammatory module observed in $Mertk^{-/-V1}$ and $Mertk^{-/-V2}$ $Tyro3^{-/-V2}$ mice, primarily to RPE cells. In addition to RNA-seq analysis, we used Luminex multiplexed cytokine array analyses on P25 lysates of RPE obtained from $Mertk^{-/-V1}$, $Mertk^{-/-V2}$ $Tyro3^{-/-V2}$, and B6 WT mice. This assay demonstrated elevated levels of the chemokine/cytokines CXCL10, CCL12, CCL19, and IL-5 in $Mertk^{-/-V1}$ and $Mertk^{-/-V2}$ $Tyro3^{-/-V2}$ RPE lysates by comparison to their B6 WT counterparts (Fig. 3J). Thus, an RPE-intrinsic inflammation is a feature of the severe, early-onset PR degeneration.

What leads to RPE inflammation in $Mertk^{-/-V1}$ and $Mertk^{-/-V2}$ $Tyro3^{-/-V2}$ mice? PR degeneration in $Mertk^{-/-V1}$ mice has historically been associated with distortion of POSs and subretinal debris buildup due to a drastic reduction in POS fragments uptake. Thus, a priori, RPE inflammation may be thought of as an obligate consequence of reduced phagocytosis. Instead, we posit that RPE inflammation distinct from deficient phagocytosis drives severe, early-onset PR degeneration. Given that $Mertk^{-/-V2}$ mice do not phenocopy the severe, early-onset inflammation, we hypothesized that it would not display RPE inflammation despite defective phagocytosis. To quantitate phagocytosis, we counted the number of rhodopsin-positive phagosomes in randomly chosen fields across all regions within RPE flat mounts in $Mertk^{-/-V2}$ and B6 WT mice. Phagosomes were quantified 1 hour after light onset, when phagosome load in B6 WT RPE is at its peak. The diameter of a POS fragment is estimated to be ~1 μm (27). Therefore, we quantified the number of rhodopsin-positive phagosomes with diameter ≥0.9 μm within RPE cells as a proxy for phagosomes that contain undigested and thus most likely recently engulfed, outer segment tips. In addition, we counted rhodopsin-positive phagosomes ≥0.5 μm in diameter for phagosomes containing intact and digested or partially digested outer segment tips. We determined the level of phagocytosis at P25, an age when retinal histology was yet unaffected (Fig. 1). The means ± SEM from B6 WT RPE was 41.9 ± 4.3 undigested ≥0.9-μm POS phagosomes (Fig. 4A). $Mertk^{-/-V2}$ RPE, by contrast, had 24.6 ± 3.0 undigested POS phagosomes (Fig. 4A). Quantification of all rhodopsin-positive phagosomes ≥0.5 μm in diameter revealed that, while B6 WT RPE had 168.1 ± 4.31 rhodopsin-positive phagosomes, in $Mertk^{-/-V2}$ RPE, the number of phagosomes was 113.1 ± 7.63. When considering ≥0.5-μm phagosomes, we noted

that their numbers within the $Mertk^{-/-V2}$ RPE were heterogeneous within an individual eye, with the number of phagosomes ranging from a maximum of 261.68 per field to a lowest of 34.09 per field. By contrast, a maximum of 259.20 per field to a minimum of 96.87 per field were observed in B6 WT RPE (Fig. 4A).

We also tested the $Mertk^{-/-V2}$ mice for engulfment of rhodopsin-positive phagosomes at 3 months of age. B6 WT RPE contained 53.4 ± 4.19 undigested ≥0.9-μm POS phagosomes at 1 hour after light onset (Fig. 4B). In stark contrast, $Mertk^{-/-V2}$ RPE had only 2.93 ± 0.395 undigested POS phagosomes. Similarly, rhodopsin-positive phagosomes ≥0.5 μm in diameter were 152 ± 8.63 in B6 WT RPE but only 46.8 ± 3.66 in $Mertk^{-/-V2}$ RPE (Fig. 4B). At 3 months of age, the numbers of phagosomes/field in $Mertk^{-/-V2}$ RPE were no longer heterogeneous, consistent with a progressive phagocytosis deficiency worsening from P25 to 3 months of age. The size and distribution of $Mertk^{-/-V2}$ RPE cells were indistinguishable from B6 WT controls at both P25 and 3 months of age as assessed by F-actin staining (fig. S4). Collectively, our results demonstrate a significant reduction in phagocytosis of outer segment tips by the RPE in $Mertk^{-/-V2}$ mice in comparison to RPE in B6 WT mice.

Despite this deficit in phagocytosis, $Mertk^{-/-V2}$ retina did not exhibit expansion of CD45$^+$ cells nor activation of CD45$^+$CD11b$^+$CD64$^+$ microglia or infiltration of CD45$^+$ CD11b$^+$-CD64$^-$ monocytes at P25 (Fig. 5A). The number of CD45$^+$ cells was statistically no different in $Mertk^{-/-V2}$ retina than in B6 WT retina and unlike the expansion and activation observed in $Mertk^{-/-V2}$ $Tyro3^{-/-V2}$ retina (Fig. 5A). Correspondingly, there was no statistically significant change in microglial activation marker expression in $Mertk^{-/-V2}$ retina relative to B6 WT retina (Fig. 5B). Luminex multiplexed cytokine array analyses did not show enhanced amounts of CXCL10, CCL12, CCL19, MCSF, and LIF in lysates from $Mertk^{-/-V2}$ neural retina and RPE as detected in $Mertk^{-/-V1}$ and $Mertk^{-/-V2}$ $Tyro3^{-/-V2}$ retina and RPE at P25 (Fig. 5C). Only CCL19 was higher in the $Mertk^{-/-V2}$ retina-RPE lysate than that in B6 WT, albeit not to the same level as in $Mertk^{-/-V1}$ and $Mertk^{-/-V2}$ $Tyro3^{-/-V2}$ retina and RPE, while all other cytokines/chemokines in $Mertk^{-/-V2}$ retina-RPE lysate were not significantly different that in B6 WT neural retina and RPE (Fig. 5C). GSEA of RPE RNA-seq data and qPCR analyses revealed that $Mertk^{-/-V2}$ mice failed to exhibit increased inflammation as $Mertk^{-/-V1}$ and $Mertk^{-/-V2}$ $Tyro3^{-/-V2}$ RPE at P25 (Fig. 5, D and F). GSEA revealed that inflammatory pathways, such as IL-6–JAK–STAT3 (signal transducer and activator of transcription 3) and TNF-α/nuclear factor κB signaling, were down-regulated in $Mertk^{-/-V2}$ RPE as compared to either $Mertk^{-/-V1}$ or $Mertk^{-/-V2}$ $Tyro3^{-/-V2}$ RPE at P25 (Fig. 5D). The $Mertk$ paralog $Tyro3$ was shown to have a role in RPE phagocytosis in vitro (17). Quantitative reverse transcription PCR validation of $Ifit1$, $Iigp1$, and $Rsad2$ confirmed the lack of heightened inflammatory response in $Mertk^{-/-V2}$ or $Tyro3^{-/-V1}$ RPE relative to B6 WT, distinctly opposed to the exacerbated inflammatory response in $Mertk^{-/-V1}$ or $Mertk^{-/-V2}$ $Tyro3^{-/-V2}$ RPE (Fig. 5F). We also examined features of inflammation in $Tyro3^{-/-V1}$ retina and failed to detect any significant changes compared to B6 WT (Fig. 5, A to C, E, and F).

$Itgb5^{-/-}$ mice provide an alternative model for studying the consequences of POS fragments uptake defects. We previously reported examination of in vivo phagocytosis in 3- to 4-month-old mice, which revealed the complete absence of the burst of POS
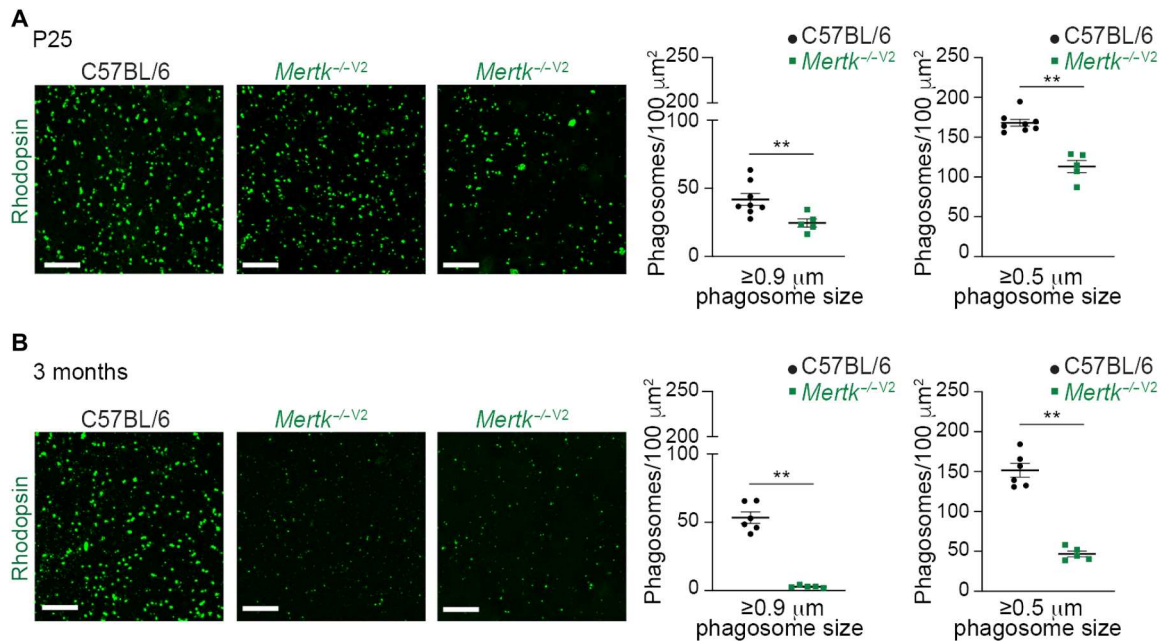
Fig. 4. Loss of *Mertk* results in early-onset defects in RPE POS phagocytosis in vivo. (**A**) POS phagocytosis analyzed by counting rhodopsin-positive inclusions in whole-mount RPE from P25 C57BL/6 WT and *Mertk*[−/−V2] mice at 1 hour after light onset. Representative images of one C57BL/6 WT and two different *Mertk*[−/−V2] mice and quantification of large phagosomes (recently engulfed POS; diameter, ≥0.9 μm) and total phagosomes (diameter, ≥0.5 μm). Means ± SEM of 13 to 16 fields per mouse, *n* = 5 to 8 mice per genotype, Mann-Whitney's test. Scale bars, 20 μm. (**B**) POS phagocytosis analyzed by counting rhodopsin-positive inclusions in whole-mount RPE from 3-month-old C57BL/6 WT and *Mertk*[−/−V2] mice at 1 hour after light onset. Representative images of one C57BL/6 WT and two different *Mertk*[−/−V2] mice and quantification of large phagosomes (recently engulfed POS fragments; diameter, ≥0.9 μm) and total phagosomes (diameter, ≥0.5 μm). Means ± SEM of 16 fields per mouse, *n* = 5 to 6 mice per genotype, Mann-Whitney's test. Scale bars, 20 μm. **P < 0.01.

phagocytosis after light onset in *Itgb5*^{−/−} RPE that is characteristic to RPE in WT mice in response to the circadian shedding of POS fragments (*14*). In vitro phagocytosis assays confirmed a defect in POS fragment recognition and thus POS fragment engulfment in primary cultures of RPE cells from *Itgb5*^{−/−} mice (*14*). We therefore examined the whole-genome transcriptional profile of *Itgb5*^{−/−} RPE by RNA-seq. We found that expression of the paired *Itgb5* and *Itgav* subunits were detected in RPE as early as P10 (fig. S5A). Unlike in *Mertk*[−/−V2] *Tyro3*[−/−V2] and *Mertk*[−/−V1] RPE, no inflammatory gene expression profile was observed in *Itgb5*^{−/−} mice as compared to control WT[129] mice at P25 (fig. S5, B and C). Together, these results indicate that phagocytic defects in RPE and reduced POS fragments uptake do not obligatorily result in the RPE inflammation associated with severe, early-onset PR degeneration. Instead, RPE inflammation was exclusively associated with the genetic deletion of *Mertk* and the concomitant hypomorphic expression/simultaneous ablation of *Tyro3* and not with the genetic deletion of *Mertk* alone or of *Tyro3* alone.

Up-regulation of inflammation-associated gene module in *Mertk*[−/−V1] and *Mertk*[−/−V2] *Tyro3*[−/−V2] RPE precedes eye opening

We next investigated whether RPE inflammation can be temporally resolved from deficient phagocytosis in *Mertk*[−/−V1] and *Mertk*[−/−V2] *Tyro3*[−/−V2] mice. Phagocytosis of POS fragments is minimal in rodents before eye-opening at P10 (*26*). We first examined whether *Mertk* and *Tyro3* expression is detected at P10, before eye-opening. We observed that both *Mertk* and *Tyro3* are expressed

in B6 WT RPE, as detected by qPCR, at P10 (Fig. 6A). Next, we analyzed the expression of inflammation-associated genes at this developmental stage by qPCR. Even at P10, *Mertk*[−/−V1] and *Mertk*[−/−V2] *Tyro3*[−/−V2] RPE cells were found to up-regulate expression of genes involved in the response to proinflammatory cytokines IFN-α, IFN-γ, and TNF-α, by comparison with B6 WT RPE (Fig. 6, B and C). Namely, we observed an ~1.5- to 2.5-fold change in the expression of IFN-stimulated genes, including *Gm4951*, *Irf7*, *Irf9*, *Rsad2*, *Ifit3*, and *Mx1* in *Mertk*[−/−V1] and *Mertk*[−/−V2] *Tyro3*[−/−V2] RPE relative to B6 WT RPE (Fig. 6, B and C). Similarly, TNF-α response genes such as *Lif* and *Tnfsf9* were up-regulated ~1.5- to 2-fold in *Mertk*[−/−V1] and *Mertk*[−/−V2] *Tyro3*[−/−V2] RPE compared to B6 WT RPE (Fig. 6, B and C). We also detected significantly increased expression (~2- to 4.5-fold) of genes encoding for the chemokines *Ccl2* and *Ccl3* in *Mertk*[−/−V1] and *Mertk*[−/−V2] *Tyro3*[−/−V2] RPE relative to B6 WT RPE (Fig. 6, B and C). These results demonstrate that RPE inflammation precedes eye-opening. The early onset of RPE inflammation in the absence of *Mertk* and reduced expression/absence of *Tyro3* is thus unlikely to be a consequence of accumulated damage in the retina as a corollary of failed RPE phagocytosis.

RPE inflammatory response precedes microglial activation and subsequently cascades to involve other immune cells

The order in which an inflammatory response occurs in RPE, microglia, and monocytes during severe, early-onset PR degeneration remains unclear. For example, microglial activation and consequent contribution to PR degeneration was shown in the RCS rat (*26*).
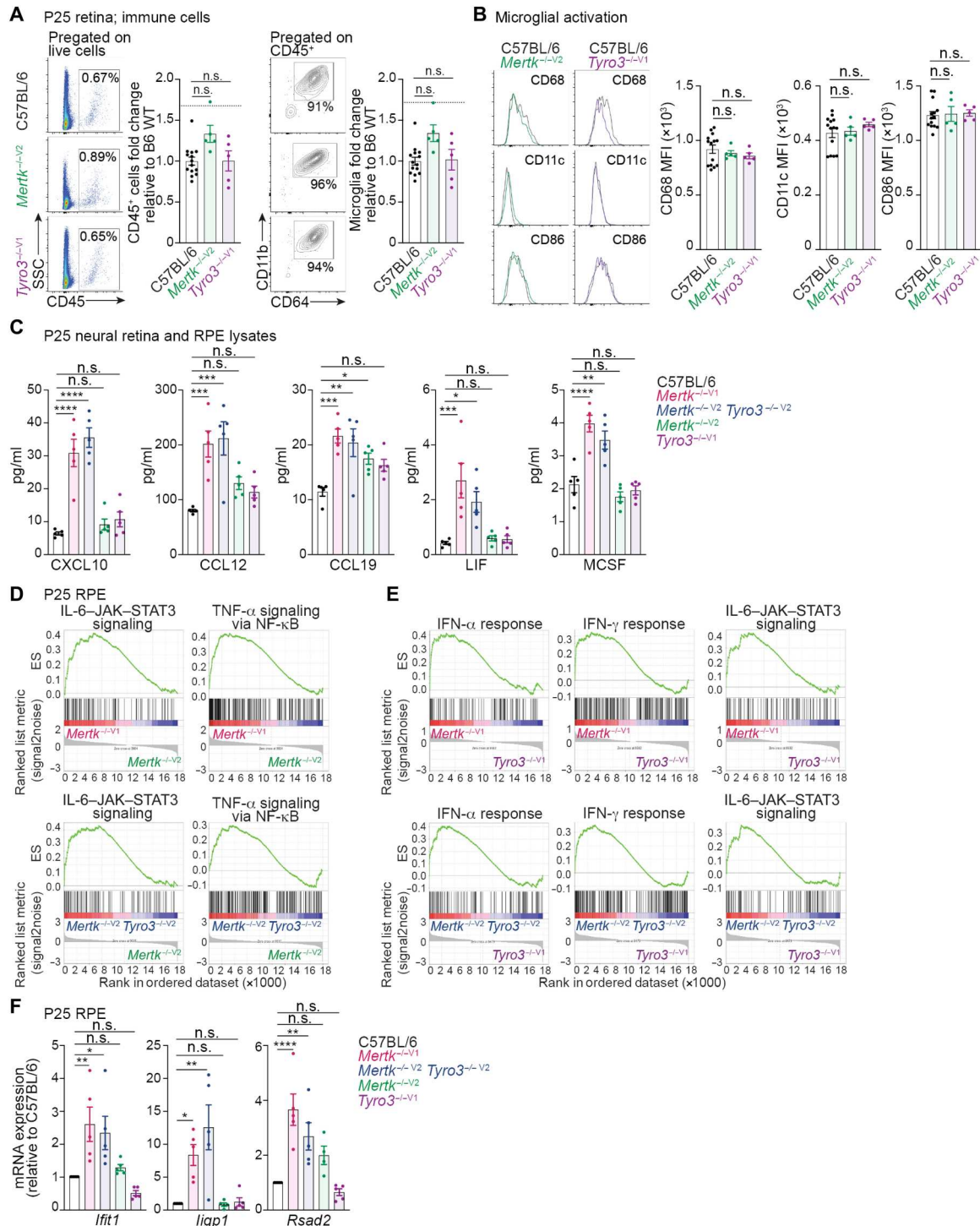
Fig. 5. Independent ablation of _Mertk_ or _Tyro3_ does not lead to retinal inflammation. (**A**) Number of CD45^{+} cells and microglia (CD45^{+}CD11b^{+}CD64^{+} cells) in P25 C57BL/6 WT, _Mertk_[−/−V2], and _Tyro3_[−/−V1] retina, determined by flow cytometry. Represented as fold change versus C57BL/6 WT. $n = 5$ to 14 per group, ANOVA. Dotted line: fold change of CD45^{+} cells and microglia observed in P25 _Mertk_[−/−V2] _Tyro3_[−/−V2] versus C57BL/6 WT (corresponding to Fig. 2C). (**B**) Microglial expression of CD68, CD11c, and CD86 and corresponding quantification of MFI. $n = 5$ to 14 per group, ANOVA. (**C**) Quantification of chemokines and cytokines in neural retinas and RPE lysates of P25 C57BL/6 WT, _Mertk_[−/−V1], _Mertk_[−/−V2] _Tyro3_[−/−V2], _Mertk_[−/−V2], and _Tyro3_[−/−V1] mice by Luminex. Represented as fold change versus C57BL/6 WT. $n = 5$ per genotype, ANOVA, Dunnet's test. Datasets from _Mertk_[−/−V1] and _Mertk_[−/−V2] _Tyro3_[−/−V2] mice correspond to data in Fig. 2F. All measurements were done in parallel. (**D** and **E**) GSEA comparing (**D**) _Mertk_[−/−V1] versus _Mertk_[−/−V2]-derived RPE (top) or _Mertk_[−/−V2] _Tyro3_[−/−V2] versus _Mertk_[−/−V2]-derived RPE (bottom) or (**E**) _Mertk_[−/−V1] versus _Tyro3_[−/−V1]-derived RPE (top) or _Mertk_[−/−V2] _Tyro3_[−/−V2] versus _Tyro3_[−/−V1]-derived RPE (bottom) at P25. (**F**) qPCR validation of inflammation-associated genes in P25 _Mertk_[−/−V1], _Mertk_[−/−V2] _Tyro3_[−/−V2], _Mertk_[−/−V2], and _Tyro3_[−/−V1] versus C57BL/6 WT RPE. Represented as fold change versus C57BL/6 WT. $n = 5$ per genotype, ANOVA, Dunnet's test. Bar graphs represent means ± SEM. n.s., *$P < 0.05$, **$P < 0.01$, ***$P < 0.001$, and ****$P < 0.0001$.
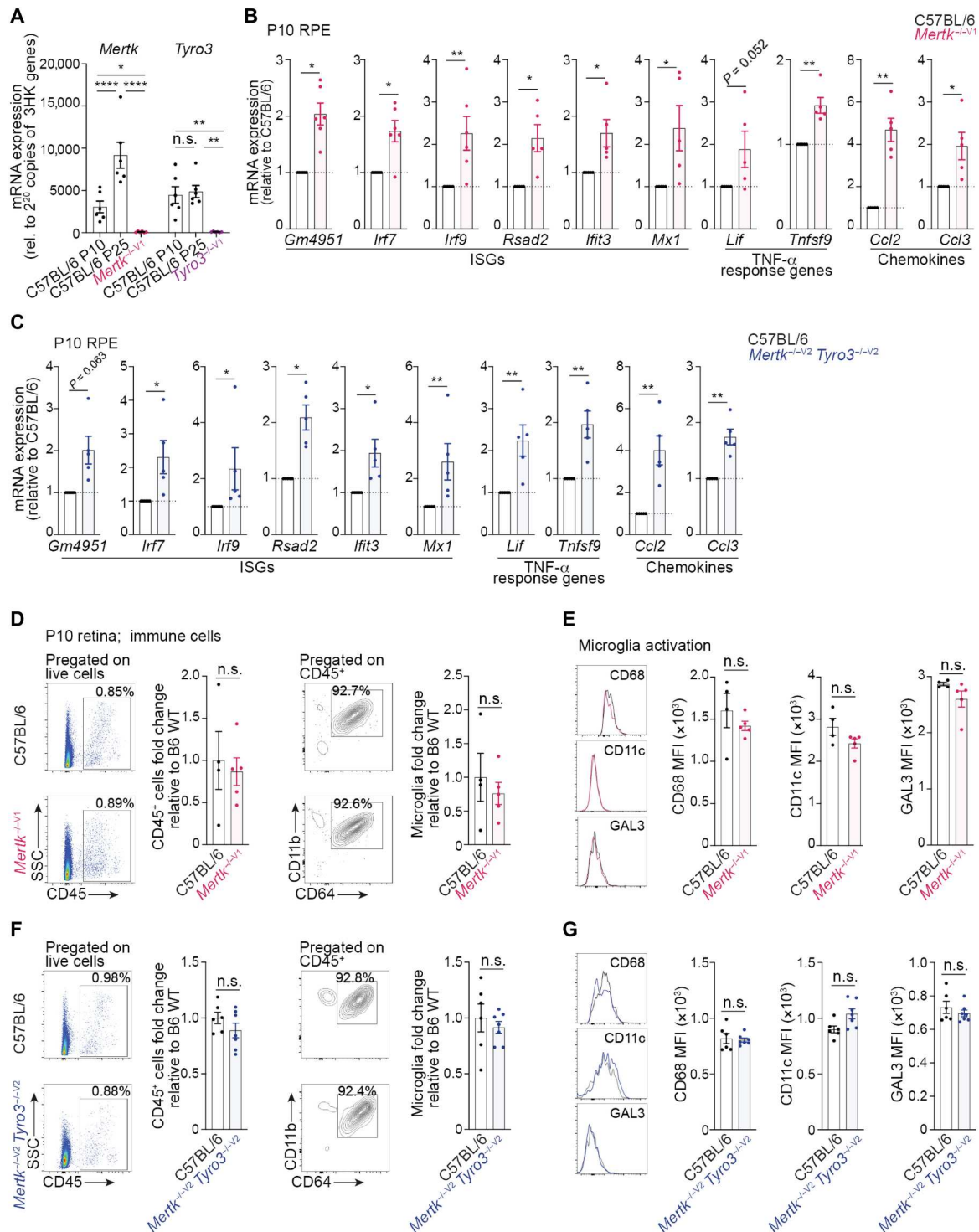
Fig. 6. Increased inflammation in the RPE of *Mertk*−/−V1** and *Mertk*−/−**V2** *Tyro3*−/−**V2** mice precedes eye-opening and retinal microglia activation.** (**A**) *Mertk* and *Tyro3* mRNA expression at P10 and P25 in C57BL/6 WT RPE by qPCR. $n = 6$ per group, ANOVA, Tukey's test. (**B** and **C**) IFN-stimulated genes (ISGs), TNF-α–inducible genes and chemokines at P10 from C57BL/6 WT and *Mertk*−/−V1 RPE ($n = 5$ to 6 per group, one-tailed Mann-Whitney's test) and C57BL/6 WT and *Mertk*−/−V2 *Tyro3*−/−V2 RPE ($n = 5$ per group, one-tailed Mann-Whitney's test), determined by qPCR. (**D**) Number of CD45+ cells and microglia (CD45+CD11b+CD64+ cells) in P10 C57BL/6 WT and *Mertk*−/−V1 retina, determined by flow cytometry. Represented as fold change versus C57BL/6 WT. $n = 4$ to 5 per group, Mann-Whitney's test. (**E**) Microglial expression of CD68, CD11c, and GAL3 and corresponding MFI quantification in C57BL/6 WT and *Mertk*−/−V1 mice at P10. $n = 4$ to 5 per group, Mann-Whitney's test. (**F**) Number of CD45+ cells and microglia in P10 C57BL/6 WT and *Mertk*−/−V2 *Tyro3*−/−V2 retina, determined by flow cytometry. Represented as fold change versus C57BL/6 WT. $n = 6$ to 7 per group, Mann-Whitney's test. (**G**) Microglial expression of CD68, CD11c, and GAL3 and corresponding MFI quantification. $n = 6$ to 7 per group, Mann-Whitney's test. Bar graphs represent means ± SEM. n.s., *$P < 0.05$, **$P < 0.01$, and ****$P < 0.0001$.

However, it was also reported that the transcriptional reprogramming of retinal microglia from a homeostatic gene expression profile to the up-regulation of injury response genes confers protection to the RPE in models of acute light damage or the autosomal dominant knock-in rhodopsin mutation model of chronic damage (28). Therefore, microglial activation due to PR damage may be protective for RPE, but RPE inflammation causing microglial activation may cause PR degeneration. To identify the nucleating event for retinal inflammation associated with severe, early-onset PR degeneration, we determined the temporal sequence of microglial versus RPE inflammation. We tested whether changes in microglial response in the neural retina were also already observed at P10 simultaneously with RPE inflammation or whether inflammatory changes were unique to RPE cells at this early age. We collected retinal samples from mice at P10 and performed flow cytometry analysis for microglia. We did not find a significant difference in the number of CD45$^+$ cells and of microglia in the neural retinas of *Mertk*$^{-/-V1}$ and *Mertk*$^{-/-V2}$ *Tyro3*$^{-/-V2}$ mice, compared to B6 WT controls at P10 (Fig. 6D, F). Moreover, the expression level of markers associated with activation (CD68, CD11c, and GAL3) was statistically no different in microglia isolated from *Mertk*$^{-/-V1}$ and *Mertk*$^{-/-V2}$ *Tyro3*$^{-/-V2}$ retinas relative to B6 WT controls (Fig. 6, E and G). Thus, at P10, the inflammatory response was confined to the RPE.

Together, our data suggest that inflammation is already present at P10, but it is restricted to the RPE. At P25, not only is inflammation detectable in the RPE, but it also extends beyond the RPE to manifest as expansion of microglial numbers and activation. By 6 weeks, unrestrained inflammation in the RPE and retinal microglia, and the resulting damage, leads to infiltration of monocytes into the retina. Thus, inflammation and retinal damage may constitute a feedback loop in the *Mertk*$^{-/-V1}$ and *Mertk*$^{-/-V2}$ *Tyro3*$^{-/-V2}$ retinas that perpetuate and exacerbate each other.

Loss of *Mertk* function in microglia, with preserved *Mertk* and *Tyro3* in RPE, does not result in severe, early-onset PR degeneration

Our temporal assessment of the retinal inflammatory response could not unequivocally rule out the possibility that subthreshold changes in the microglia in the absence of *Mertk* may precipitate RPE inflammation at P10. In addition, failed POS fragments uptake due to the absence of microglial phagocytosis in *Mertk*$^{-/-V1}$ and *Mertk*$^{-/-V2}$ *Tyro3*$^{-/-V2}$ mice may drive RPE inflammation, as well as the inflammatory response of microglia and monocytes, in these mice. Although the loss of *Mertk* alone does not culminate in severe, early-onset PR degeneration as would be anticipated for a primarily microglia-driven phenotype, we attempted to definitively rule out the role of microglia in being the sole driver of the *Mertk*$^{-/-V1}$ and *Mertk*$^{-/-V2}$ *Tyro3*$^{-/-V2}$ mice phenotype. First, we confirmed MERTK expression in microglia isolated from the retina by flow cytometry. Albeit at lower levels of expression than in brain microglia, retinal microglia expressed an ample amount of MERTK (Fig. 7A). Next, we generated mice bearing conditional ablation of *Mertk* in myeloid, *Csf1r*$^+$ cells (*Csf1r-cre*$^+$ *Mertk*$^{f/f}$ mice). We confirmed that MERTK amounts were significantly reduced in *Csf1r-cre*$^+$ *Mertk*$^{f/f}$ mice when compared to littermate *Csf1r-cre*$^-$ *Mertk*$^{f/f}$ mice (fig. S6). We then collected retinas from these mice at P25 and performed flow cytometry analysis to test whether the

conditional genetic ablation of *Mertk* altered the number and/or the activation state of microglia. We found no significant changes in the number of CD45$^+$ cells and of microglia in the neural retinas of *Csf1r-cre*$^+$ *Mertk*$^{f/f}$ mice, compared to *Csf1r-cre*$^-$ *Mertk*$^{f/f}$ littermate controls (Fig. 7B). In addition, the expression level of markers associated with activation (CD68, CD11c, and CD86) was statistically unchanged in *Csf1r-cre*$^+$ *Mertk*$^{f/f}$ microglia, compared to *Csf1r-cre*$^-$ *Mertk*$^{f/f}$ controls (Fig. 7C). Furthermore, histological analysis of eyes obtained from 12-month-old *Csf1r-cre*$^+$ *Mertk*$^{f/f}$ mice showed preserved histoarchitecture of all retinal layers (Fig. 7D). Collectively, our results show that the loss of microglia-intrinsic function of *Mertk* with intact *Mertk* and *Tyro3* in the RPE does not give rise to early-onset retinal degeneration, in contrast to what was observed in *Mertk*$^{-/-V2}$ *Tyro3*$^{-/-V2}$ or *Mertk*$^{-/-V1}$ mice. Loss of *Mertk* in the microglia does not drive microglial activation in the absence of RPE inflammation. Therefore, the loss of MERTK function in microglia is either dispensable for the retinal degeneration phenotype or is, at least, not sufficient for inducing retinal degeneration. A microglia-intrinsic function of this RTK remains a formal possibility, if it is to amplify a response initiating outside microglia, such as in the RPE.

Pharmacological inhibition of JAK kinase activity significantly inhibits PR cell death and preserves ONL thickness

The observation that a broad-spectrum type I and type II IFN and IL-6 response characterizes the incipient RPE inflammation led us to test whether inhibition of JAK-STAT signaling, a key effector of the type I and II IFN and IL-6 response, could at least partially prevent the PR degeneration in *Mertk*$^{-/-V1}$ mice. Ruxolitinib is an FDA-approved, selective JAK1/2 inhibitor (29, 30). Ruxolitinib is known to preferentially partition into milk, reaching a milk: plasma mean concentration ratio of 13.4:1 (drugs.com). To initiate ruxolitinib treatment, ruxolitinib (2 g/kg)–containing chow were fed to *Mertk*$^{-/-V1}$ or B6 WT dams starting at day 10 after parturition so that it is passed on to suckling pups. Weaned pups were continued on ruxolitinib chow until either P25 or P30 (Fig. 8A). As controls, nursing dams and their weaned pups were fed standard diet. Following this regimen of ruxolitinib treatment and control, we tested target inhibition in the pups (Fig. 8B). Pups were euthanized at P25, mRNA was isolated from RPE, and expression of selected genes was measured by qPCR. These results demonstrate that 15 days on ruxolitinib significantly decreased JAK1/2-driven expression of inflammatory genes such as *Ifit1*, *Tgtp1*, and *Gm4951* in the RPE of the pups, by comparison with no treatment (Fig. 8B). Having confirmed target validation, we performed H&E staining on retinal sections at P30 and quantitated the thickness of the ONL in WT B6 and *Mertk*$^{-/-V1}$ mice with or without ruxolitinib treatment (Fig. 8C). While ONL thickness was reduced ~35% in *Mertk*$^{-/-V1}$ mice without ruxolitinib treatment, by comparison to untreated B6 WT mice, ONL thickness was reduced only by ~15% in *Mertk*$^{-/-V1}$ mice treated with ruxolitinib, by comparison to untreated B6 WT mice (Fig. 8C). Thus, ruxolitinib treatment resulted in a statistically significant, ~2-fold less degeneration of the ONL in *Mertk*$^{-/-V1}$ mice. As an alternate method for quantifying PR loss, we also counted rows of PR nuclei of the ONL. B6 WT mice had 10.67 ± 0.13 rows of ONL nuclei, while standard chow–treated *Mertk*$^{-/-V1}$ mice had 6.89 ± 0.06 rows of ONL nuclei, i.e., ~40% reduction in the number of ONL nuclei. By contrast, ruxolitinib-
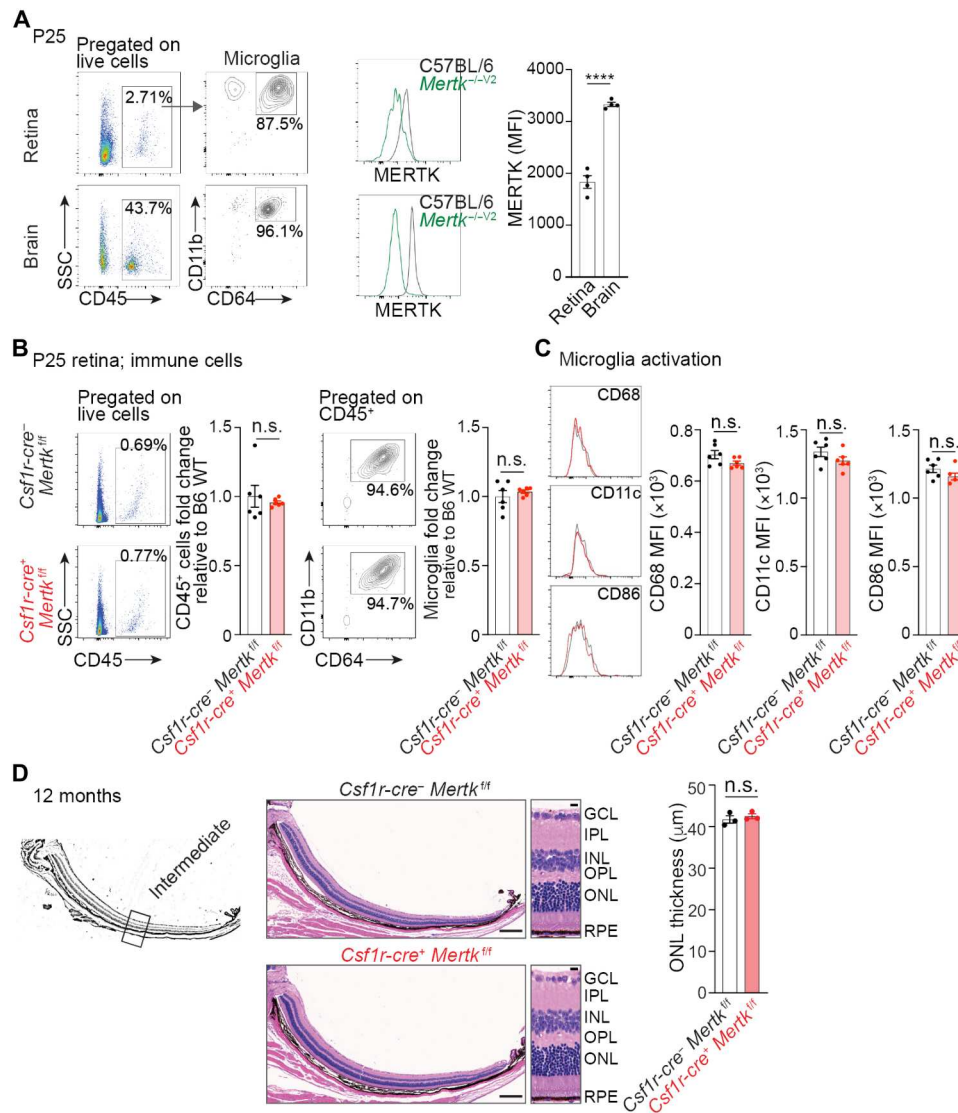
Fig. 7. Conditional ablation of *Mertk* in microglia is not sufficient to drive retinal degeneration. (**A**) P25 C57BL/6 WT and *Mertk*$^{-/-V2}$ retina and brain tissue stained and analyzed for MERTK expression by flow cytometry. Gating strategy for identification of microglia (CD45$^+$CD11b$^+$CD64$^+$ cells) in the retina (top) and the brain (bottom). Representative MERTK expression and quantification of MFI on the surface of retina and brain microglia are shown. *n* = 4 mice per group, Mann-Whitney's test. (**B**) Number of CD45$^+$ cells and microglia (CD45$^+$CD11b$^+$CD64$^+$ cells) in P25 *Csf1r-cre*$^+$ *Mertk*$^{f/f}$ and *Csf1r-cre*$^-$ *Mertk*$^{f/f}$ retina, determined by flow cytometry. Represented as fold change versus *Csf1r-cre*$^-$ *Mertk*$^{f/f}$ mice. *n* = 6 mice per group, Mann-Whitney's test. (**C**) Microglial expression of CD68, CD11c, and GAL3 and corresponding MFI quantification in *Csf1r-cre*$^+$ *Mertk*$^{f/f}$ and *Csf1r-cre*$^-$ *Mertk*$^{f/f}$ mice at P25. *n* = 6 mice per group, Mann-Whitney's test. (**D**) Schematic of transversal section of the retina indicating the intermediate region wherein ONL thickness was quantified. Retinal sections were stained with H&E. Representative retinal sections and quantification of ONL thickness. Ten measurements per mouse, *n* = 3 mice per genotype. Mann-Whitney's test. Scale bars, 200 μm (whole section) and 10 μm (inset). Bar graphs represent means ± SEM. n.s. and ****P < 0.0001.

treated *Mertk*$^{-/-V1}$ mice had 8.33 ± 0.38 rows of ONL nuclei, i.e., ~20% reduction in the number of ONL nuclei (Fig. 8C). Again, ruxolitinib-treated *Mertk*$^{-/-V1}$ mice exhibited ~2-fold less degeneration. Collectively, both forms of quantification demonstrate that the dose (2 g/kg) and regimen (from P10 to P30) of ruxolitinib used significantly lessened the severity of the *Mertk*$^{-/-V1}$ retinal degeneration, albeit PR loss was not entirely prevented.

We also quantitated the pyknotic nuclei within the ONL of *Mertk*$^{-/-V1}$ mice fed on standard or ruxolitinib chow as a measure of dying PR (Fig. 8D). These results showed that there was an ~4-fold reduction in the number of pyknotic nuclei with

ONL of *Mertk*$^{-/-V1}$ mice with ruxolitinib treatment, by comparison to untreated *Mertk*$^{-/-V1}$ mice (Fig. 8D). Thus, subduing RPE inflammation by inhibition of JAK1/2 activity at least partially but significantly reduces the severity of the aggressive, early-onset PR degeneration phenotype observed in *Mertk*$^{-/-V1}$ mice.
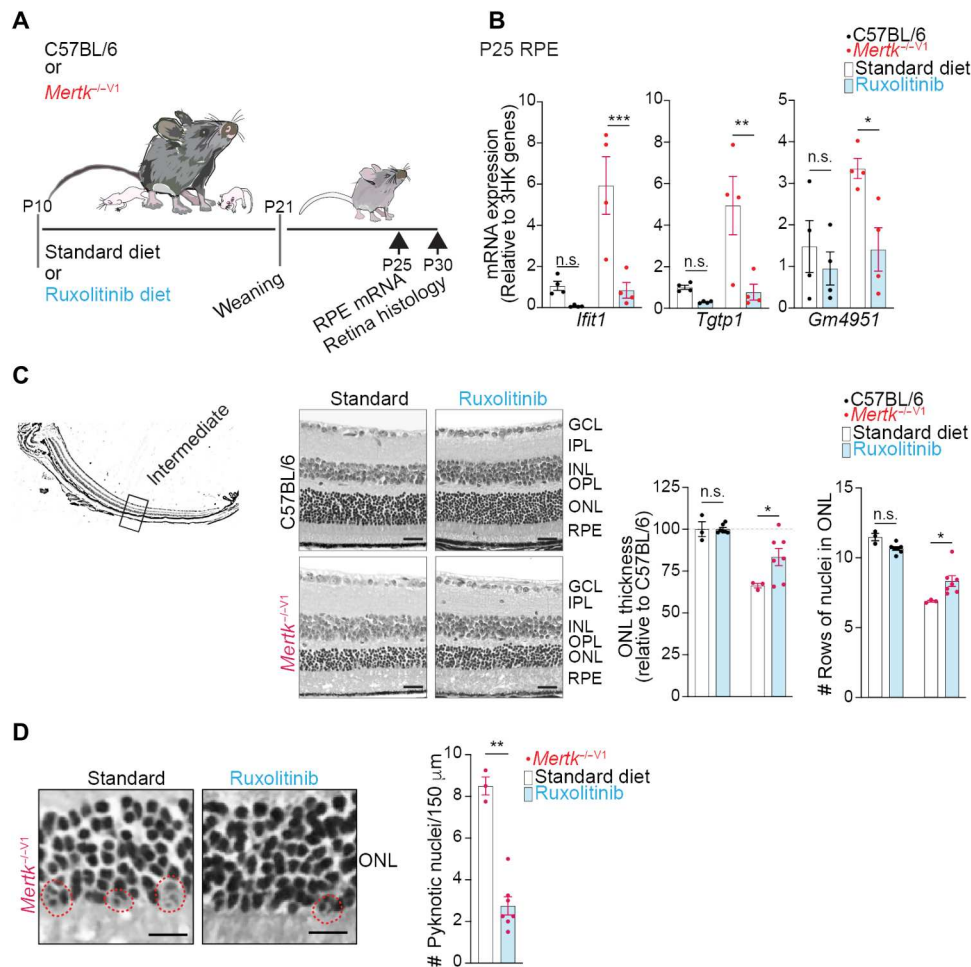
Fig. 8. The selective JAK1/2 inhibitor ruxolitinib significantly prevents early-onset PR death. (A) Diagram showing experimental design. C57BL/6 WT and $Mertk^{-/-V1}$ dams were fed a standard or ruxolitinib-containing diet (2 g of ruxolitinib/kg of chow) from the time pups were at P10 until weaning at P21. Weanlings continued to receive standard or ruxolitinib-containing diet until the indicated times of sample collection. RPE samples were collected at P25 for mRNA expression of target genes. Eyes were collected at P30 to study retinal histology. **(B)** Inflammation-associated genes in P25 RPE by qPCR. $n = 4$ mice per condition, two-way ANOVA. **(C)** Schematic of transversal section of the retina indicating the intermediate region wherein ONL thickness was quantified. Retina sections were collected at P30, stained with H&E and ONL thickness and number of rows of nuclei within ONL were quantified. Representative retina sections from C57BL/6 WT and $Mertk^{-/-V1}$ mice treated with standard or ruxolitinib diet. $n = 3$ to 7 mice per condition, two-way ANOVA. Scale bars, 20 μm. **(D)** Representative images and quantification of the number of pyknotic nuclei in ONL of P30 $Mertk^{-/-V1}$ mice treated with ruxolitinib or standard diet. $n = 3$ to 7 mice per condition, Mann-Whitney's test. Scale bars, 10 μm. Bar graphs represent means ± SEM. n.s., $*P < 0.05$, $**P < 0.01$, and $***P < 0.001$.

DISCUSSION

Severe, early-onset PR degeneration due to MERTK deficiency is associated with RPE inflammation, microglial activation, and monocyte infiltration into the retina

RP associated with *MERTK* mutations is a severe, early-onset form of this disease. It has been speculated that RP with *MERTK* mutations is associated with inflammation; nonetheless, the role of inflammation in disease etiology was less clear. Here, we show that *Mertk* and *Tyro3* function redundantly as negative regulators of inflammation in the mouse RPE. Mice lacking WT expression of *Mertk* and hypomorphic expression/loss of *Tyro3* displayed a broad-spectrum RPE inflammatory response including type I and II IFN response, IL-6 signaling pathway gene expression, and TNF-α response gene expression. Microglial activation was also a characteristic of retinal inflammation in $Mertk^{-/-V1}$ mice and phenocopied in $Mertk^{-/-V2}$ $Tyro3^{-/-V2}$ mice. Both these mouse models were also associated with monocyte infiltration into the retina. This cascading inflammation culminated in severe, early-onset retinal degeneration. By contrast, mouse models of defective phagocytosis that were not associated with RPE inflammation, such as $Mertk^{-/-V2}$ mice or the phenotype of the $Itgb5^{-/-}$ (*14*) mice, presented with an age-dependent onset and progressive changes such as thinning of the peripheral retina. The requirement for ablating both *Mertk* and *Tyro3* RTKs is reminiscent of a similar need for simultaneous deletion of the TAM ligands *Gas6* and *Pros1* in severe, early-onset PR degeneration (*31*). Thus, RPE inflammatory response may be a crucial feature of at least a subset of *MERTK* mutation–associated RP.

Inflammation is not a consequence of failed phagocytosis

Inflammation, heretofore, has been mostly considered a secondary consequence of failed phagocytosis, accumulation of damaged and

degraded POS fragments, and the death of PRs. We showed recently that neural retina–resident microglia are already activated in RCS rat at an age before detectable PR death and debris buildup (26). Here, our characterization of the inflammatory response in the RPE itself revealed that not only does RPE inflammation precede retinal degeneration but also that the inception of RPE inflammation happens before eye opening in mouse pups, a time when phagocytosis is expected to be minimal (26). If RPE inflammation was to be only a consequence of a failure to clear POS fragment debris and accumulation of dead PR, then such a process can be expected to lag the primary defect in phagocytosis. A gradual process of buildup of POS fragments and dead PRs would progressively culminate in RPE inflammation. Instead, we observe the opposite, i.e., histological changes in the retina trail the initial RPE inflammatory response. We also observe that inflammation and PR degeneration are not merely obligatory consequences of defective phagocytosis. This notion is supported by the finding that loss of function of the phagocytic receptor *Itgb5* did not phenocopy the inflammation observed in *Mertk*$^{-/-V1}$ or *Mertk*$^{-/-V2}$ *Tyro3*$^{-/-V2}$ mice. While only minimal RPE inflammation was seen in *Mertk*$^{-/-V2}$ mice, RPE from these mice were deficient in phagocytosis. *Mertk*$^{-/-V2}$ mice had demonstrable phagocytosis defects in their macrophages as well, consistent with the phagocytic function of MERTK (22). Neither did we observe increased inflammation in the *Tyro3*$^{-/-V1}$ RPE, although TYRO3 is reportedly involved in POS fragments phagocytosis (17). *Itgb5*$^{-/-}$, *Mertk*$^{-/-V2}$, or *Tyro3*$^{-/-V1}$ mice do not develop severe, early-onset PR degeneration (14, 22, 32). Thus, impaired peak phagocytosis is not intrinsically associated with an enhanced inflammatory response gene expression and PR degeneration. Consistent with this idea, a previous study had demonstrated that the ectopic expression of another phagocytic receptor BAI-1 in *Mertk*$^{-/-V1}$ mice failed to prevent or reduce PR degeneration (33). MERTK and TYRO3 not only participate in phagocytosis but also function in the negative regulation of inflammation (34). These RTKs have not only a Grb2-binding motif that is functionally essential for their phagocytic function (35) but also a distinct immunoreceptor tyrosine-based inhibitory motif (34). Our results indicate that RPE homeostasis requires the redundant function of these RTKs for the negative regulation of inflammation. It will be interesting to ascertain the individual roles of mutating these motifs in MERTK and TYRO3 in determining the severe, early-onset PR degeneration phenotype associated with the loss of *Mertk* and the hypomorphic expression/loss of *Tyro3*.

RPE versus microglial inflammation as the nucleating event for PR degeneration

Although microglia (and even other myeloid cells) are involved in a cascading inflammatory response within the retina, leading to PR degeneration, we and others have demonstrated that the severe, early-onset PR degeneration phenotype in *Mertk*$^{-/-V1}$ and *Mertk*$^{-/-V2}$ *Tyro3*$^{-/-V2}$ mice requires both the loss of *Mertk* and the concomitant hypomorphic expression/simultaneous genetic ablation of *Tyro3* (17, 22). While *Mertk* is expressed in microglia and widely in myeloid cells (34), *Tyro3* expression has only been described in very specific myeloid populations such as CD11c$^+$ PDL2$^+$ dendritic cells involved in the inhibition of type 2 immunity, such as in asthma or allergic diseases (36). Therefore, we hypothesized that rather than microglia or myeloid cells, inflammation associated with severe, early-onset PR degeneration likely nucleates in

a tissue that expresses both *Mertk* and *Tyro3*. This made us investigate RPE inflammation. Two pieces of independent evidence support the RPE as one of the initial sites of an inflammatory response culminating in severe, early-onset PR degeneration. First, RPE inflammation was detected at P10, before microglial activation. Second, the *Csf1r*-cre–dependent genetic ablation of *Mertk*, which ablates this RTK in microglia and in myeloid cells, did not result in an inflammatory response and retinal degeneration. However, it is evident that microglial activation is a part of the inflammatory response that occurs as a reaction to microglia-extrinsic inflammation. Wang *et al.* (37) first demonstrated that tamoxifen administration selectively inhibits microglia in the murine retina through yet to be defined molecular pathways. Their and other studies have further shown that tamoxifen-mediated microglia inhibition improves retinal integrity and function in mouse models of retinal degeneration, such as bright light damage and the rd10 strain (37, 38). In our previous study on MERTK-deficient RCS rats, inhibition of retinal microglial activation with tamoxifen delayed retinal degeneration, although the efficacy of tamoxifen was moderate (26). These studies illustrate the common involvement of microglia in retinal diseases with different causes and etiologies. Whether RPE inflammation is also shared among different forms of retinal degeneration, and, if so, whether targeting RPE inflammation would be more effective than targeting microglia, is as yet unexplored. A head-to-head comparison of targeting RPE nucleated inflammation via ruxolitinib versus microglial activation by tamoxifen in RCS rats or in *Mertk*$^{-/-V1}$ and *Mertk*$^{-/-V2}$ *Tyro3*$^{-/-V2}$ mice or testing a combination approach has not yet been done.

The primordial trigger of inflammation, however, remains undiscovered. The visual cycle is intrinsically associated with inflammation. Following photobleaching, rod cells return to their basal state as all-trans-retinal is removed from disk membranes, cyclic guanosine 3′,5′-monophosphate is resynthesized, and rhodopsin is regenerated from 11-cis-retinal and opsin (39–41). The RPE plays a role in uptake of all-trans-retinol transported out of POS fragments and its isomerization into 11-cis-retinol followed by its oxidization to 11-cis-retinal. Mutations in genes encoding transporters such as *ABCA4* involved in the elimination of all-trans-retinal from PRs are known to cause macular degeneration, rod-cone dystrophies, or RP (42, 43). All-trans-retinal has also been reported to activate the NLRP3 inflammasome and cause RPE death (44). Thus, RPE cells can be expected to require anti-inflammatory mechanisms for the uptake and recycling of inflammatory products of the visual cycle eliminated by the PRs, such as all-trans-retinol. Spontaneous electrical activity in the retina has been reported before eye-opening (45) indicating that phototoxic damage and the requirement to keep inflammation at bay may be expected to be required quite early in development. Still, we cannot rule out the loss of negative regulation of inflammation in other cell types expressing both *Mertk* and *Tyro3*, such as Müller glia, as the genesis that spills over to the RPE.

Inflammation as the target of therapy in severe, early-onset RP due to MERTK mutation

The molecular characteristic of RPE inflammation afflicting *Mertk*$^{-/-V1}$ or *Mertk*$^{-/-V2}$ *Tyro3*$^{-/-V2}$ mice was enhanced type I and II IFN, IL-6, and TNF-α signaling. The pathogenic role of TNF-α in *Mertk* loss of function in murine RP was previously ruled out (23). Both type I and II IFN and IL-6 pathways are

dependent on the JAK kinases, JAK1/2. We tested whether JAK1/2 inhibition would ameliorate the severe, early-onset PR degeneration. A treatment regimen with ruxolitinib from P10 to P30 significantly reduced PR death and the shrinking of the ONL. Whether administration of ruxolitinib earlier would provide improved benefit and more protection against PR degeneration is yet to be determined. Collectively, our results demonstrate that, in the absence of $Mertk$ and deficits of $Tyro3$, a nascent JAK1/2-STAT–dependent inflammatory response pathway within RPE leads to a panoply of cytokines and chemokines, microglia activation and migration, and, eventually, a runaway cascade of inflammatory response involving the infiltration of monocytes, to culminate in severe, early-onset PR degeneration. Whether other modifiers influence an incipient RPE inflammatory response in RCS rat or in human patients with RP remains to be investigated. Furthermore, the nature of the inflammatory response and whether it is amenable to therapeutic targeting as in $Mertk^{-/-V1}$ mice remain unknown. The presence of $MERTK$ mutations that do not result in severe, early-onset RP appears to indicate that modifiers determine the severity and age of onset of $MERTK$ mutation–associated RP. If modifiers of $MERTK$-associated RP phenotype govern an inflammatory component responsible for severe, early-onset retinal degeneration, then inhibiting this inflammatory axis may provide a promising, tractable avenue for therapeutic benefits.

MATERIALS AND METHODS

Experimental design
This study was designed to identify the pathological drivers of early-onset PR degeneration in mice with genetic ablation of $Mertk$ and $Tyro3$. We used transcriptional, histological, immunological, and functional analysis of RPE and retina. We used mice at different ages, ranging from P10 to 12-month-old mice. We tested the efficacy of the FDA-approved JAK1/2 inhibitor ruxolitinib in the prevention of early-onset retinal degeneration in mice with loss of $Mertk$ and hypomorphic expression of $Tyro3$. Experiments were independently replicated, and, for each experiment, an $n > 4$ for each group, unless otherwise indicated in the figure legends, was used.

Animals
Animals were bred and maintained under a strict 12-hour light cycle and fed with standard chow diet in a specific pathogen–free facility at the Yale University. All animal experiments were performed in accordance with regulatory guidelines and standards set by the Institutional Animal Care and Use Committee of Yale University and Fordham University. C57BL/6J mice were purchased from the Jackson Laboratory (strain no. 000664) and subsequently bred and housed at the Yale University. $Mertk^{-/-V1}$ mice have been described previously (22, 46, 47). The generation of $Mertk^{-/-V2}$ and $Mertk^{-/-V2}$ $Tyro3^{-/-V2}$ mice is described by Akalu et $al.$ (22). $Tyro3^{-/-V1}$ mice have also been described previously (47). $Mertk^{-/-V1}$, $Mertk^{-/-V2}$, and $Mertk^{-/-V2}$ $Tyro3^{-/-V2}$ mice, as well as $Csf1r$-cre $Mertk^{f/f}$ mice (bearing conditional ablation of $Mertk$ in myeloid cells) (48), were bred and housed at the Yale University. Previously described (14) $Itgb5^{-/-}$ mice and strain-matched 129T2/SvEmsJ WT controls (Jackson Laboratory, strain no. 002065) were bred and housed at Fordham University. Genotyping of selected animals of the various aforementioned $Mertk$, $Tyro3$, or $Itgb5$ genotypes in our colonies showed them all to be negative for the $rd8$ mutation. Genome-wide single-nucleotide polymorphism analysis for $Mertk^{-/-V2}$ mice determined that ~84.37% of the genome in $Mertk^{-/-V2}$ mice corresponded to C57BL/6J and ~15.62% to C57BL/6NJ (22).

Total RNA isolation and sequencing analysis
RNA was collected from P25 mice using a previously validated method (49). Briefly, after euthanasia, mice were enucleated, and the posterior eyecup was incubated on ice in 200 μl of RNAprotect (Qiagen) for 1 hour. RPE containing tubes were agitated for 10 min to dislodge any RPE cells attached to the posterior eyecup and centrifuged for 5 min at 685g. The RPE pellet was then subjected to total RNA extraction using an RNeasy Mini kit (Qiagen) following the manufacturer's instructions.

RNA libraries were prepared at the Yale Keck Biotechnology Resource Laboratory from three to six biological replicates per condition. Samples were sequenced using 150–base pair paired-end reading on a NovaSeq 6000 instrument (Illumina). RNA-seq datasets from P25 RPE obtained from C57BL/6, $Mertk^{-/-V1}$, and $Mertk^{-/-V2}$ mice are available through the Gene Expression Omnibus (GEO) under accession ID: GSE205070 (22). Datasets corresponding to P25 RPE from $Mertk^{-/-V2}$ $Tyro3^{-/-V2}$, $Tyro3^{-/-V1}$, $Igtb5^{-/-}$, and WT[129] mice are available through GEO under accession ID: GSE214005. The raw reads were then subjected to trimming by btrim (50) to remove sequencing adaptors and low-quality regions. Next, reads were mapped to the mouse genome (GRCm38) using STAR (51). Last, the DEseq2 (52) package was run to identify DEGs according to P values adjusted for multiple comparisons. Genes with P-adjusted values less than 0.05 and $\log_2$fold change ≤ -1.25 or ≥ 1.25 were considered differentially expressed. These data were subsequently represented in a heatmap generated by Qlucore Omics Explorer. Volcano plots were generated using GraphPad Prism (GraphPad Software Inc.). We also subjected normalized counts of all genes from various samples to GSEA (53, 54). The hallmark gene set database was used to determine which pathways are enriched in our samples. Resulting pathways that had high normalized enrichment scores and false discovery rate (FDR) Q value < 0.05 were reported.

GSEA allows for testing whether a set of genes determined a priori shows statistically significant, concordant differences between two samples (54). There are three portions in each plot. The top portion shows the enrichment scores (ES). The middle portion displays where the individual hits in the set appear in the ranked list of genes. The bottom portion plots the value of the ranking metric as the analysis moves down the list of ranked genes.

qPCR analysis
Reverse transcription of RNA was performed using the iScript cDNA Synthesis Kit (Bio-Rad). Using the KAPA SYBR Fast qPCR Kit (Kapa Biosystems), we amplified cDNA fragments and proceeded with qPCR reactions on CFX96 Thermal Cycler Real Time System (Bio-Rad). The reactions were normalized to three housekeeping genes ($Gapdh$, $Hprt$, and $Rn18s$), and specificity of the amplified products was verified by looking at the dissociation curves. All oligonucleotides for qPCR were either purchased from Sigma-Aldrich or produced at the Yale University Keck Oligonucleotide Synthesis Facility (see sequences in table S1).

Luminex cytokine assay

Eyes from P25 mice were obtained. Neural retinas were subsequently separated from posterior eyecups, and both tissues were incubated on ice in radioimmunoprecipitation assay buffer with protease inhibitor cocktail, EDTA-free (Sigma-Aldrich Inc.), for up to 1 hour. Next, posterior eyecups were removed, and the dislodged RPE cells were combined with corresponding neural retinas and sonicated for 20 s on ice. After 10 min at 14,000 rpm in a refrigerated centrifuge, supernatants were transferred to new tubes. Undiluted supernatants from $n = 5$ mice per genotype were then tested for expression of 44 different cytokines and chemokines on the Mouse Cytokine 44-Plex Discovery Array (Eve Technologies). RPE lysates were also tested independently for cytokine expression using the same platform. The values for all measurements obtained in these arrays can be found in table S2.

Histological analysis

After euthanasia by carbon dioxide inhalation, eyecups were immediately collected and incubated overnight in eye fixative (Service-Bio). H&E staining was performed by iHisto Inc. Samples were processed, embedded in paraffin, and sectioned at 4 μm. Paraffin sections were then deparaffinized and hydrated using the following steps: 15 min in xylene twice; 5, 5, and 5 min in 100, 100, and 75% ethanol, respectively; and 5 min in 1× phosphate-buffered saline (PBS) at room temperature repeated three times. After deparaffinization, 4-μm sectioned samples were placed on glass slides and stained with H&E. Whole-slide scanning (20×) was performed on an EasyScan Infinity (Motic). ONL thickness was analyzed in ImageJ [National Institutes of Health (NIH)]. Quantification of ONL thickness was performed in the central, medial, or peripheral portions of the retina, as indicated in the corresponding figure legends. The areas analyzed were defined by distance from the optic disk. Ten to 15 measurements of ONL thickness were done per mouse. PR length, the combined length of inner and outer PR segments, was quantified and averaged from 10 measurements from two to three eye sections per mouse using ImageJ (NIH).

Immunofluorescence

For IBA1 staining, 4-μm paraffin sections were deparaffinized at 65°C for 20 min and incubated in xylenes for 5 min twice. Sections were subsequently incubated in 100% ethanol (two times for 5 min), 95% ethanol (two times for 3 min), 70% ethanol (3 min), and 5 min in PBS at room temperature. Epitope unmasking was performed using citrate buffer [10 mM citric acid and 0.05% Tween 20 (pH 6)] for 10 min in the microwave (10% total power). Sections were then blocked in PBS and 1% bovine serum albumin with 0.01% Triton-X100 for 30 min at room temperature and incubated overnight at 4°C with primary antibody anti-IBA1 (1:400, Thermo Fisher Scientific, catalog no. NC1718288). After washing, samples were incubated with donkey anti-rabbit Alexa Fluor 488–conjugated secondary antibody (1:500, Thermo Fisher Scientific) for 1 hour at room temperature and mounted on slides using 4′,6-diamidino-2-phenylindole (DAPI)–containing mounting medium (Vector Laboratories). Image acquisition was performed using a Leica Stellaris 8 confocal microscope using an oil immersion ×40 objective. The layers of the retina were delineated using DAPI, and the number of IBA1+ cells was counted within each layer (inner nuclear layer, OPL, and ONL). Images were analyzed using ImageJ software (NIH).

ERG recordings

All experimental animals were adapted in a dark room for 12 hours before recordings. Animals were anesthetized under dim red illumination using a ketamine (100 mg/kg) and xylazine (10 mg/kg) cocktail injected intraperitoneally, and pupils were dilated by application of a 0.5% tropicamide eye drop (Sandoz) at least 15 min before recordings. The cornea was intermittently irrigated with balanced salt solution to maintain the baseline recording and prevent keratopathy. Scotopic ERGs were acquired with the UTAS ERG System with a BigShot Ganzfeld Stimulator (LKC Technologies Inc.). A needle reference electrode was placed under the skin of the back of the head, a ground electrode was attached subcutaneously to the tail, and a lens electrode was placed in contact with the central cornea. The scotopic response was recorded for different luminances (i.e., log −2.1, −0.6, 0.4, and 1.4 cd·s/m^2) using EMWin software, following the manufacturer's instructions (LKC Technologies Inc.). The a-wave was measured as the difference in amplitude between baseline recording and the trough of the negative deflection, and the b-wave amplitude was measured from the trough of the a-wave to the peak of the ERG.

Whole-mount RPE preparation, labeling, and in situ phagosome quantification

Quantification of POS phagosomes in whole-mount RPE in situ was performed as described previously (55). Tissues were collected immediately postmortem from 3-month-old mice euthanized at 1 and 7 hours after light onset ($n = 5$ of each genotype). Posterior eyecups were dissected and fixed for 30 min in 4% paraformaldehyde in PBS. Radial cuts were made to flatten tissues before labeling with rhodopsin monoclonal antibody B6-30 (Abcam, catalog no. ab230692) (56) and AlexaFluor 488–conjugated donkey anti-mouse secondary antibody. Counterstains labeling nuclei with DAPI and F-actin with Alexa Fluor 594–conjugated phalloidin (Thermo Fisher Scientific) served to indicate cell orientation and integrity. A Leica TSP8 confocal system was used to acquire x-y image stacks at 0.25-μm intervals to cover the thickness of the entire RPE depth from the basal aspect of nuclei to apical microvilli of the RPE. Thirteen to 16 fields were imaged for each specimen with a field size of 186.5 μm by 186.5 μm. Fields were spaced along the dorsoventral and nasotemporal retinal meridians. Maximal projections of z stacks of equal thickness were used to quantify POS phagosomes defined by rhodopsin-positive structures of ≥0.5 or 0.9 μm diameter using ImageJ.

Flow cytometry staining and acquisition

The method used to isolate and immunophenotype the retina was previously described (57). Briefly, retinas were digested for 1 hour at 37°C with agitation in RPMI (Gibco) containing collagenase A (1.5 mg/ml; Roche) and deoxyribonuclease I (0.4 mg/ml; Sigma-Aldrich). For adult P42 mice, retinas were collected after intracardiac perfusion with saline solution. Single-cell suspensions of tissues were then stained in PBS with Zombie viability dye (BioLegend) for 10 min. Cells were then incubated in 2% fetal calf serum/PBS solution containing anti-mouse CD16/32 antibody (BioLegend, clone 93) for 15 min and subsequently stained with a combination of fluorophore-conjugated primary antibodies against mouse CD45 (BioLegend, clone 30-F11), CD11b (BioLegend, clone M1/70), CD64 (BioLegend, clone X54-5/7.1), Ly6C (BioLegend, clone HK1.4), Ly6G (BioLegend, clone 1A8), CD68

(BioLegend, clone FA-11), galectin-3 (BioLegend, clone M3/38), CD11c (BioLegend, clone N418), and CD86 (BioLegend, clone GL-1) at 4°C for 25 min. After staining, cells were washed and fixed in 1% paraformaldehyde in PBS. Data were acquired with BD LSRII flow cytometer using BD FACSDiva software (BD Biosciences). Last, raw data were analyzed using FlowJo software (Tree Star Inc.).

Ruxolitinib treatment

Ruxolitinib is an FDA-approved, selective JAK1/2 inhibitor used to treat intermediate- or high-risk myelofibrosis (*29*). Ruxolitinib was administered to C57BL/6 or $Mertk^{-/-V1}$ mice, by providing ruxolitinib-supplemented chow (2 g/kg, Research Diets) ad libitum to the nursing dams starting at P10 (pups received the drug indirectly through breast milk) and, after that, directly to the experimental mice from weaning (P21) until euthanasia. Control littermates were manipulated identically but received standard chow (Envigo) throughout the duration of the experiments. RPE samples were collected at P25 for mRNA studies or at P35 for histological evaluation.

Statistical analysis

All statistical analyses were done using GraphPad Prism (GraphPad Software Inc.). All data are shown as means ± SEM, and each data point represents a unique animal. Statistical differences between experimental groups were determined by using nonparametric tests, namely, one- and two-tailed Mann-Whitney test, two-tailed Student's *t* test, and one-way and two-way analysis of variances (ANOVAs).

Supplementary Materials

This PDF file includes:
Figs. S1 to S6
Table S1

Other Supplementary Material for this manuscript includes the following:
Table S2
Data S1

View/request a protocol for this paper from *Bio-protocol.*

REFERENCES AND NOTES

1. S. Ferrari, E. Di Iorio, V. Barbaro, D. Ponzin, F. S. Sorrentino, F. Parmeggiani, Retinitis pigmentosa: Genes and disease mechanisms. *Curr. Genomics* **12**, 238–249 (2011).

2. C. Hamel, Retinitis pigmentosa. *Orphanet J. Rare Dis.* **1**, 40 (2006).

3. I. Audo, S. Mohand-Said, E. Boulanger-Scemama, X. Zanlonghi, C. Condroyer, V. Démontant, F. Boyard, A. Antonio, C. Méjécase, S. El Shamieh, J.-A. Sahel, C. Zeitz, MERTK mutation update in inherited retinal diseases. *Hum. Mutat.* **39**, 887–913 (2018).

4. C. Parinot, E. F. Nandrot, A comprehensive review of mutations in the MERTK proto-oncogene. *Adv. Exp. Med. Biol.* **854**, 259–265 (2016).

5. M. Tschernutter, S. A. Jenkins, N. H. Waseem, Z. Saihan, G. E. Holder, A. C. Bird, S. S. Bhattacharya, R. R. Ali, A. R. Webster, Clinical characterisation of a family with retinal dystrophy caused by mutation in the Mertk gene. *Br. J. Ophthalmol.* **90**, 718–723 (2006).

6. C. L. McHenry, Y. Liu, W. Feng, A. R. Nair, K. L. Feathers, X. Ding, A. Gal, D. Vollrath, P. A. Sieving, D. A. Thompson, *MERTK* arginine-844-cysteine in a patient with severe rod-cone dystrophy: Loss of mutant protein function in transfected cells. *Invest. Ophthalmol. Vis. Sci.* **45**, 1456–1463 (2004).

7. J. E. Dowling, R. L. Sidman, Inherited retinal dystrophy in the rat. *J. Cell Biol.* **14**, 73–109 (1962).

8. M. H. Chaitin, M. O. Hall, Defective ingestion of rod outer segments by cultured dystrophic rat pigment epithelial cells. *Invest. Ophthalmol. Vis. Sci.* **24**, 812–820 (1983).

9. P. M. D'Cruz, D. Yasumura, J. Weir, M. T. Matthes, H. Abderrahim, M. M. LaVail, D. Vollrath, Mutation of the receptor tyrosine kinase gene Mertk in the retinal dystrophic RCS rat. *Hum. Mol. Genet.* **9**, 645–651 (2000).

10. E. Nandrot, E. M. Dufour, A. C. Provost, M. O. Péquignot, S. Bonnel, K. Gogat, D. Marchant, C. Rouillac, B. Sépulchre de Condé, M.-T. Bihoreau, C. Shaver, J. L. Dufier, C. Marsac, M. Lathrop, M. Menasche, M. M. Abitbol, Homozygous deletion in the coding sequence of the *c-mer* gene in RCS rats unravels general mechanisms of physiological cell adhesion and apoptosis. *Neurobiol. Dis.* **7**, 586–599 (2000).

11. W. Feng, D. Yasumura, M. T. Matthes, M. M. LaVail, D. Vollrath, Mertk triggers uptake of photoreceptor outer segments during phagocytosis by cultured retinal pigment epithelial cells. *J. Biol. Chem.* **277**, 17016–17022 (2002).

12. J. L. Duncan, M. M. LaVail, D. Yasumura, M. T. Matthes, H. Yang, N. Trautmann, A. V. Chappelow, W. Feng, H. S. Earp, G. K. Matsushima, D. Vollrath, An RCS-like retinal dystrophy phenotype in mer knockout mice. *Invest. Ophthalmol. Vis. Sci.* **44**, 826–838 (2003).

13. A. Gal, Y. Li, D. A. Thompson, J. Weir, U. Orth, S. G. Jacobson, E. Apfelstedt-Sylla, D. Vollrath, Mutations in *MERTK*, the human orthologue of the RCS rat retinal dystrophy gene, cause retinitis pigmentosa. *Nat. Genet.* **26**, 270–271 (2000).

14. E. F. Nandrot, Y. Kim, S. E. Brodie, X. Huang, D. Sheppard, S. C. Finnemann, Loss of synchronized retinal phagocytosis and age-related blindness in mice lacking alphavbeta5 integrin. *J. Exp. Med.* **200**, 1539–1545 (2004).

15. Y. Chang, S. C. Finnemann, Tetraspanin CD81 is required for the αvβ5-integrin-dependent particle-binding step of RPE phagocytosis. *J. Cell Sci.* **120**, 3053–3063 (2007).

16. D. Prasad, C. V. Rothlin, P. Burrola, T. Burstyn-Cohen, Q. Lu, P. Garcia de Frutos, G. Lemke, TAM receptor function in the retinal pigment epithelium. *Mol. Cell. Neurosci.* **33**, 96–108 (2006).

17. D. Vollrath, D. Yasumura, G. Benchorin, M. T. Matthes, W. Feng, N. M. Nguyen, C. D. Sedano, M. A. Calton, M. M. LaVail, *Tyro3* modulates *Mertk*-associated retinal degeneration. *PLOS Genet.* **11**, e1005723 (2015).

18. E. F. Nandrot, M. Anand, D. Almeida, K. Atabai, D. Sheppard, S. C. Finnemann, Essential role for MFG-E8 as ligand for αvβ5 integrin in diurnal retinal phagocytosis. *Proc. Natl. Acad. Sci. U.S.A.* **104**, 12005–12010 (2007).

19. Y. Pan, D. F. Geisert, W. E. Orr, E. E. Geisert, The effects of a CD81 null mutation on retinal pigment epithelium in mice. *Neurochem. Res.* **36**, 569–573 (2011).

20. B. K. Song, S. Levy, E. E. Geisert Jr., Increased density of retinal pigment epithelium in $cd81^{-/-}$ mice. *J. Cell. Biochem.* **92**, 1160–1170 (2004).

21. J.-Y. Kim, H. Zhao, J. Martinez, T. A. Doggett, A. V. Kolesnikov, P. H. Tang, Z. Ablonczy, C. C. Chan, Z. Zhou, D. R. Green, T. A. Ferguson, Noncanonical autophagy promotes the visual cycle. *Cell* **154**, 365–376 (2013).

22. Y. T. Akalu, M. E. Mercau, M. Ansems, L. D. Hughes, J. Nevin, E. J. Alberto, X. N. Liu, L. Z. He, D. Alvarado, T. Keler, Y. Kong, W. M. Philbrick, M. Bosenberg, S. C. Finnemann, A. Iavarone, A. Lasorella, C. V. Rothlin, S. Ghosh, Tissue-specific modifier alleles determine *Mertk* loss-of-function traits. *eLife* **11**, e80530 (2022).

23. D. M. Maddox, W. L. Hicks, D. Vollrath, M. M. LaVail, J. K. Naggert, P. M. Nishina, An ENU-induced mutation in the *Mertk* gene (Mertk^nmf12) leads to a slow form of retinal degeneration. *Invest. Ophthalmol. Vis. Sci.* **52**, 4703–4709 (2011).

24. G. Palczewska, A. Maeda, M. Golczak, E. Arai, Z. Dong, L. Perusek, B. Kevany, K. Palczewski, Receptor MER tyrosine kinase proto-oncogene (MERTK) is not required for transfer of Bis-retinoids to the retinal pigmented epithelium. *J. Biol. Chem.* **291**, 26937–26949 (2016).

25. J. Xie, Y. Li, J. Dai, Y. He, D. Sun, C. Dai, H. Xu, Z. Q. Yin, Olfactory ensheathing cells grafted into the retina of RCS rats suppress inflammation by down-regulating the JAK/STAT pathway. *Front. Cell. Neurosci.* **13**, 341 (2019).

26. D. S. Lew, F. Mazzoni, S. C. Finnemann, Microglia inhibition delays retinal degeneration due to MerTK phagocytosis receptor deficiency. *Front. Immunol.* **11**, 1463 (2020).

27. E. García-García, "Diversity in Phagocytic Signaling" in *Molecular Mechanisms of Phagocytosis* (Springer US, Boston, MA, 2005), pp. 1–22.

28. E. G. O'Koren, C. Yu, M. Klingeborn, A. Y. W. Wong, C. L. Prigge, R. Mathew, J. Kalnitsky, R. A. Msallam, A. Silvin, J. N. Kay, C. Bowes Rickman, V. Y. Arshavsky, F. Ginhoux, M. Merad, D. R. Saban, Microglial function is distinct in different anatomical locations during retinal homeostasis and degeneration. *Immunity* **50**, 723–737.e7 (2019).

29. R. A. Mesa, Ruxolitinib, a selective JAK1 and JAK2 inhibitor for the treatment of myeloproliferative neoplasms and psoriasis. *IDrugs* **13**, 394–403 (2010).

30. A. Quintás-Cardama, K. Vaddi, P. Liu, T. Manshouri, J. Li, P. A. Scherle, E. Caulder, X. Wen, Y. Li, P. Waeltz, M. Rupar, T. Burn, Y. Lo, J. Kelley, M. Covington, S. Shepard, J. D. Rodgers, P. Haley, H. Kantarjian, J. S. Fridman, S. Verstovsek, Preclinical characterization of the selective JAK1/2 inhibitor INCB018424: Therapeutic implications for the treatment of myeloproliferative neoplasms. *Blood* **115**, 3109–3117 (2010).

31. T. Burstyn-Cohen, E. D. Lew, P. G. Traves, P. G. Burrola, J. C. Hash, G. Lemke, Genetic dissection of TAM receptor-ligand interaction in retinal pigment epithelial cell phagocytosis. *Neuron* **76**, 1123–1132 (2012).

32. E. D. Lew, J. Oh, P. G. Burrola, I. Lax, A. Zagórska, P. G. Través, J. Schlessinger, G. Lemke, Differential TAM receptor-ligand-phospholipid interactions delimit differential TAM bioactivities. *eLife* **3**, e03385 (2014).

33. K. K. Penberthy, C. Rival, L. S. Shankman, M. H. Raymond, J. Zhang, J. S. A. Perry, C. S. Lee, C. Z. Han, S. Onengut-Gumuscu, K. Palczewski, J. J. Lysiak, K. S. Ravichandran, Context-dependent compensation among phosphatidylserine-recognition receptors. *Sci. Rep.* **7**, 14623 (2017).

34. C. V. Rothlin, E. A. Carrera-Silva, L. Bosurgi, S. Ghosh, TAM receptor signaling in immune homeostasis. *Annu. Rev. Immunol.* **33**, 355–391 (2015).

35. N. Tibrewal, Y. Wu, V. D'Mello, R. Akakura, T. C. George, B. Varnum, R. B. Birge, Autophosphorylation docking site Tyr-867 in Mer receptor tyrosine kinase allows for dissociation of multiple signaling pathways for phagocytosis of apoptotic cells and down-modulation of lipopolysaccharide-inducible NF-κB transcriptional activation. *J. Biol. Chem.* **283**, 3618–3627 (2008).

36. P. Y. Chan, E. A. Carrera Silva, D. De Kouchkovsky, L. D. Joannas, L. Hao, D. Hu, S. Huntsman, C. Eng, P. Licona-Limón, J. S. Weinstein, D. R. Herbert, J. E. Craft, R. A. Flavell, S. Repetto, J. Correale, E. G. Burchard, D. G. Torgerson, S. Ghosh, C. V. Rothlin, The TAM family receptor tyrosine kinase TYRO3 is a negative regulator of type 2 immunity. *Science* **352**, 99–103 (2016).

37. X. Wang, L. Zhao, Y. Zhang, W. Ma, S. R. Gonzalez, J. Fan, F. Kretschmer, T. C. Badea, H.-H. Qian, W. T. Wong, Tamoxifen provides structural and functional rescue in murine models of photoreceptor degeneration. *J. Neurosci.* **37**, 3294–3310 (2017).

38. C. Gargini, E. Terzibasi, F. Mazzoni, E. Strettoi, Retinal organization in the retinal degeneration 10 (rd10) mutant mouse: A morphological and ERG study. *J. Comp. Neurol.* **500**, 222–238 (2007).

39. M. E. Burns, D. A. Baylor, Activation, deactivation, and adaptation in vertebrate photoreceptor cells. *Annu. Rev. Neurosci.* **24**, 779–805 (2001).

40. V. Y. Arshavsky, T. D. Lamb, E. N. Pugh Jr., G proteins and phototransduction. *Annu. Rev. Physiol.* **64**, 153–187 (2002).

41. T. D. Lamb, E. N. Pugh Jr., Dark adaptation and the retinoid cycle of vision. *Prog. Retin. Eye Res.* **23**, 307–380 (2004).

42. V. C. Sheffield, E. M. Stone, Genomics and the eye. *N. Engl. J. Med.* **364**, 1932–1942 (2011).

43. R. K. Koenekoop, The gene for Stargardt disease, ABCA4, is a major retinal gene: A mini-review. *Ophthalmic Genet.* **24**, 75–80 (2003).

44. Y. Liao, H. Zhang, D. He, Y. Wang, B. Cai, J. Chen, J. Ma, Z. Liu, Y. Wu, Retinal pigment epithelium cell death is associated with NLRP3 inflammasome activation by all-trans retinal. *Invest. Ophthalmol. Vis. Sci.* **60**, 3034–3045 (2019).

45. A. Tiriac, B. E. Smith, M. B. Feller, Light prior to eye opening promotes retinal waves and eye-specific segregation. *Neuron* **100**, 1059–1065.e4 (2018).

46. T. D. Camenisch, B. H. Koller, H. S. Earp, G. K. Matsushima, A novel receptor tyrosine kinase, Mer, inhibits TNF-alpha production and lipopolysaccharide-induced endotoxic shock. *J. Immunol.* **162**, 3498–3503 (1999).

47. Q. Lu, M. Gore, Q. Zhang, T. Camenisch, S. Boast, F. Casagranda, C. Lai, M. K. Skinner, R. Klein, G. K. Matsushima, H. S. Earp, S. P. Goff, G. Lemke, Tyro-3 family receptors are essential regulators of mammalian spermatogenesis. *Nature* **398**, 723–728 (1999).

48. L. Bosurgi, Y. G. Cao, M. Cabeza-Cabrerizo, A. Tucci, L. D. Hughes, Y. Kong, J. S. Weinstein, P. Licona-Limon, E. T. Schmid, F. Pelorosso, N. Gagliani, J. E. Craft, R. A. Flavell, S. Ghosh, C. V. Rothlin, Macrophage function in tissue repair and remodeling requires IL-4 or IL-13 with apoptotic cells. *Science* **356**, 1072–1076 (2017).

49. C. Xin-Zhao Wang, K. Zhang, B. Aredo, H. Lu, R. L. Ufret-Vincenty, Novel method for the rapid isolation of RPE cells specifically for RNA extraction and analysis. *Exp. Eye Res.* **102**, 1–9 (2012).

50. Y. Kong, Btrim: A fast, lightweight adapter and quality trimming program for next-generation sequencing technologies. *Genomics* **98**, 152–153 (2011).

51. A. Dobin, C. A. Davis, F. Schlesinger, J. Drenkow, C. Zaleski, S. Jha, P. Batut, M. Chaisson, T. R. Gingeras, STAR: Ultrafast universal RNA-seq aligner. *Bioinformatics* **29**, 15–21 (2013).

52. M. I. Love, W. Huber, S. Anders, Moderated estimation of fold change and dispersion for RNA-seq data with DESeq2. *Genome Biol.* **15**, 550 (2014).

53. V. K. Mootha, C. M. Lindgren, K. F. Eriksson, A. Subramanian, S. Sihag, J. Lehar, P. Puigserver, E. Carlsson, M. Ridderstråle, E. Laurila, N. Houstis, M. J. Daly, N. Patterson, J. P. Mesirov, T. R. Golub, P. Tamayo, B. Spiegelman, E. S. Lander, J. N. Hirschhorn, D. Altshuler, L. C. Groop, PGC-1α-responsive genes involved in oxidative phosphorylation are coordinately downregulated in human diabetes. *Nat. Genet.* **34**, 267–273 (2003).

54. A. Subramanian, P. Tamayo, V. K. Mootha, S. Mukherjee, B. L. Ebert, M. A. Gillette, A. Paulovich, S. L. Pomeroy, T. R. Golub, E. S. Lander, J. P. Mesirov, Gene set enrichment analysis: A knowledge-based approach for interpreting genome-wide expression profiles. *Proc. Natl. Acad. Sci. U.S.A.* **102**, 15545–15550 (2005).

55. S. Sethna, T. Chamakkala, X. Gu, T. C. Thompson, G. Cao, M. H. Elliott, S. C. Finnemann, Regulation of phagolysosomal digestion by Caveolin-1 of the retinal pigment epithelium is essential for vision. *J. Biol. Chem.* **291**, 6494–6506 (2016).

56. G. Adamus, Z. S. Zam, A. Arendt, K. Palczewski, J. H. McDowell, P. A. Hargrave, Anti-rhodopsin monoclonal antibodies of defined specificity: Characterization and application. *Vision Res.* **31**, 17–31 (1991).

57. E. G. O'Koren, R. Mathew, D. R. Saban, Fate mapping reveals that microglia and recruited monocyte-derived macrophages are definitively distinguishable by phenotype in the retina. *Sci. Rep.* **6**, 20636 (2016).